ELSEVIER

A simple combustion method for the synthesis of multi-functional ZrO$_2$/CuO nanocomposites: Excellent performance as Sunlight photocatalysts and enhanced latent fingerprint detection

L. Renuka [a,c], K.S. Anantharaju [b,c,**], Y.S. Vidya [d,*], H.P. Nagaswarupa [a], S.C. Prashantha [a], S.C. Sharma [c,e], H. Nagabhushana [f,*], G.P. Darshan [g]

[a] Department of Science, Research Center, East West Institute of Technology, Bengaluru, 560091, India
[b] Department of Chemistry, Dayananda Sagar College of Engineering, Shavige Malleshwara Hills, Kumaraswamy Layout, Bengaluru, 560078, India
[c] Dr.D. Premachandra Sagar Centre for Advanced Materials, DSCE, Bengaluru, 560078, India
[d] Department of Physics, Lal Bahadur Shastry Government First Grade College, Bengaluru, 560032, India
[e] Department of Mechanical Engineering, Jain University, Jain Group of Institutions, Bengaluru, 560069, India
[f] Prof. C.N.R. Rao Centre for Advanced Materials, Tumkur University, Tumkur, 572 103, India
[g] Department of Physics, Acharya Institute of Graduate Studies, Bangalore 560 107, India

ARTICLE INFO

ABSTRACT

A facile solution combustion synthesis has been adopted to synthesize ZrO$_2$/CuO nanocomposite oxides (NCO's) by utilizing Oxalyl dihydrazide (ODH) as fuel. The X-ray diffraction patterns and TEM analysis reveals the presence of cubic ZrO$_2$ and CuO in ZrO$_2$/CuO NCO's. The NCO's synthesized by simple, fast, highly sensitive and low-cost method is found to be an alternate to traditional luminescent powders for the detection and enhancement of finger marks in a broad range of surfaces. The photoluminescence analysis indicates that the present NCO is an effective blue component in display applications. The synthesized ZrO$_2$/CuO (2:1) composite exhibited excellent photocatalytic activity towards the degradation of various dyes under Sunlight. In particular, Indigo carmine dye was chosen to explore the photocatalytic performance of prepared NCO's under Sunlight illumination. It was found that ZrO$_2$:CuO (2:1) NCO showed enhanced photocatalytic activity of 97% which was found to be 3.3 times 2.4 times and 1.5 times higher than that of pure ZrO$_2$, CuO and commercial P25. This can be mainly attributed to the balance between the parameters, band gap, nature of morphology, crystallite size, defects and surface area which causes a slow electron-hole pair recombination rate with fast electron transfer ability. It opens new window to use this simple method to synthesize multifunctional character ZrO$_2$-based composite materials in the area of photocatalysis particularly waste water treatment, display applications as well as a labeling agent to enhance latent fingerprints.

© 2017 Elsevier B.V. All rights reserved.

1. Introduction

A competent approach to environmental pollution remediation is achieved by considering primary focus on cubic ZrO$_2$ as heterogeneous photocatalysis. Zirconia (ZrO$_2$) is a well known vital multifunctional material and extremely versatile semiconductor with applications in photocatalysis as a result of its comparatively high photo-activity compared to other semiconductors. It is renowned for its mechanical properties, biocompatibility and analysis has shown that it is often utilized in dental implants or coatings on orthopedic implants like Ti metal [1,2]. On the other hand, a serious drawback is that ZrO$_2$ absorbs only 4% of solar light which was considered as a very big barrier for its practical application. In order to use effectively the solar energy, many researchers have done vast research in the field of photocatalysis and explained clearly that it is necessary to develop the visible light response of photocatalyst [3,4].

A wide range of metal oxide semiconductors TiO$_2$, ZnO and ZrO$_2$ have been investigated and reported [5–7]. However large scale applications of these semiconductors are greatly restricted. Therefore, to improve their light response, many approaches like metal

ions or non-metal ions doping, dye sensitization, preparation of composite and semiconductor doping are reported [8–10]. Several researchers targeted on mixed oxide semiconductors (MOS) due to its efficient charge separation of mixed semiconductor and a factorial transfer of photo-generated electrons and holes from one semiconductor to another [11–13]. The preparation of MOS could act as a sensitizer by shifting the absorption wavelength to the visible region [14–16]. The recombination of electron hole pair in photocatalysis is suppressed by coupling ZrO_2 with another metal oxide semiconductor. NCO's with tunable band-gap are prepared which offers an opportunity to extend the absorption wavelength from the UV to visible light region with enhanced photocatalytic activity. Due to the vast decrease in electron-hole pair recombination and enhanced visible light adsorption by composites, the photocatalytic activity has been enhanced.

ZrO_2 has been chosen for this study because of its acid −base and red-ox capabilities along with its electrical properties, thermal stability and strong mechanical strength [17,18]. Moreover from an economical point of view, the interest has been focused on 3d transition metals catalysts [19,20]. Copper is frequently chosen as the material to prepare composite due to its high activity at low-temperature and its lower cost than that of expensive metals with lower energy band gap (1.9 eV) [21–23]. Many reports are presented on the photocatalytic activity of TiO_2−ZrO_2 binary oxides for the degradation of ethylene and 4-chlorophenol under UV light [24–26]. Depending on the preparation method and calcination temperature, crystalline CuO, highly dispersed CuO and Cu^{2+} in the lattice of ZrO_2 can be identified.

Composite ZrO_2/CuO has applications as a suitable and convenient coating on orthopedic implants to forestall infection with high biocompatibility and sterile properties [27]. Yan Jian-hui and his co-workers reported CuO/ZrO_2 catalyst as a stable photo catalyst for H_2 evolution from aqueous oxalic acid solution under simulated sunlight irradiation [28]. Muhammad Ali Ehsan et al. synthesized CuO−1.5 ZrO_2 composite thin film from heteronuclear molecular complex and tested its electrocatalytic activity towards ethanol oxidation [29]. Yan Jian-hui and his co-workers reported the synthesis of CuO/ZrO_2 by solid state and co-precipitation method for photocatalytic hydrogen evaluation under simulated sunlight irradiation [30]. The combination of Zr^{IV}/Cu^{I} was demonstrated to have the ability to induce the photochemical reduction of CO_2 to CO upon the visible light induced MMCT of Zr^{IV}-O-Cu^{I} to Zr^{III}-O-Cu^{II} [31]. Metal to metal charge transfer (MMCT) is referred to as transition of electron from one type of metal to another type of metal with different oxidation state. The oxo-bridge is formed between these two different metals in a composite by absorbing light [32]. Hence this innovative work has provided some new thrust in the field of photocatalysis.

Various fabrication techniques were applied to load a metal oxide in another such as impregnation method [33], solid state dispersion method, sol–gel method [34], hydrothermal method [35], co-precipitation method, mechanical mixing method, photo-deposition method, flame spray pyrolysis etc. Whereas these methods have their own disadvantages like most of them involve prolonged, difficult procedures, require high temperature, specialized instruments, toxic reagents and external additives throughout the reaction. Among the various preparation ways available, solution combustion synthesis is an efficient and economical and homogeneous method for the preparation of various industrial MOS [36–39]. This method involves a self-sustained reaction in homogeneous solution of various oxidizers (e.g., metal nitrates) and fuels (e.g., urea, glycine, hydrazides, ODH). Solution combustion synthesis is becoming more popular and versatile methodology for the preparation of MOS. However, novel nanomaterials can be synthesized easily as meta-stable phases can be formed in short time. Highly active surface can be prepared in heterogeneous materials

easily that was helpful in transfer and separation of charge carriers [40]. This method has its own advantages such as less time for synthesis, energy efficient, molecular level mixing of raw materials, simple equipment and composition of the product can be tuned [41,42].

A fingerprint acts as the most powerful tool for identifying individuals because the ridge patterns of every print are unique and immutable [43]. Fingerprint is widely spread over many areas, including forensic investigations, safety control, individual credentials, and even medical diagnostics [44]. Thus fingerprint detection is considered as a crucible area in forensic investigation. Nowadays, this detection of hidden (latent) fingerprints is most sensitive techniques. This latent finger prints (LFPs) are invisible which must made visualized and identified [45]. This is achieved by using physical methods only on the fixed area such as powdering on the finger prints. This is of three types namely regular, metallic and luminescent. This method must be performed under proper ventilation and requires safety equipment's since toxic chemicals are used. To overcome this, application of NCO ZrO_2/CuO has been potential method in detection of latent finger print to provoke the research community.

With such a goal, in the present investigation a remarkable performance of ZrO_2/CuO NCO as an independent Sunlight induced photocatalyst for degradation of Indigo carmine (IC) dye has been observed. The composition of these NCO's has been prepared systematically by changing the ratios of both the metal oxides. The size, phase, energy band gap and luminescence for synthesized NCO's were examined by a series of physical and chemical characterization techniques and correlated to the electrochemical and photocatalytic activity. In addition, ZrO_2/CuO NCO's were employed as a labeling agent to enhance LFPs on different surfaces by a simple technique.

2. Experimental

2.1. Synthesis of ODH

Hydrazine hydrate was taken in a beaker and diethyl oxalate solution was added slowly drop by drop from burette. The mixture was continuously stirred for complete formation of ODH. Once the reaction over, the beaker was left undisturbed for one day. The top solution was decanted first and then obtained solid was squeezed in a clean white cloth to remove the water content. The obtained solid was placed in a hydrothermal autoclave maintained at 120 °C for about 10 h and calcined for 2 h at 140 °C in order to remove the remaining moisture content. Finally, the obtained ODH powder was grinded, collected and stored. Supplementary Fig. S1 depicts the pictorial representation of ODH synthesized in laboratory.

2.2. Synthesis of ZrO_2 nanoparticles

ZrO_2 nanoparticles (NPs) were prepared by solution combustion synthesis using zirconyl nitrate $[ZrO(NO_3)_2]$ as oxidizer and ODH as fuel. The stoichiometric composition of fuel and oxidizer were calculated using propellant chemistry principle, with fuel to oxidizer ratio to be unity. The fuel and oxidizer were taken in cylindrical crucible and minimum quantity of water was added and stirred to get homogeneity. This crucible was placed in a muffle furnace preheated at 500 °C. Initially, solution boils and dehydration takes place followed by removal of gases like N_2, CO_2 and H_2O removed as water vapour, finally NPs were obtained [46].

2.3. Synthesis of CuO nanoparticle

The above said procedure was adopted to synthesize CuO nanoparticle, instead of $ZrO(NO_3)_2$, $Cu(NO_3)_2$ was used.

2.4. Synthesis of ZrO_2/CuO NCO's

Zirconyl nitrate and Cupric nitrate $Cu(NO_3)_2$ in the ratio 1:1 and required amount of ODH fuel was added in the cylindrical crucible. Minimum quantity of double distilled water was added and stirred for about ten min to attain homogeneity. Then the procedure mentioned above was followed to synthesize NCO. The synthesized NCO was labelled as ZrCu. Similarly, zirconyl nitrate and cupric nitrate in the ratio 1:2 and 2:1 were synthesized by following the same procedure and labelled as $ZrCu_2$ and Zr_2Cu respectively. The steps involved in the synthesis of NCO's were depicted in Supplementary Fig. S2.

2.5. Characterization

At an accelerating voltage of 300KV, HRTEM studies were carried out on a TECNAIF (model T-30) S- twin high resolution transmission electron microscope to know the internal morphology and crystalline size and with help of SEM, Hitachi-3000, the surface morphology of synthesized samples was observed. FT-IR was performed in the range of 4000–400 cm^{-1} with the help of Perkin Elmer FTIR (Spectrum-1000) spectrometer in order to identify the functional groups present in the sample. UV–vis absorption spectrum was recorded using SL 159 ELICO UV–vis spectrophotometer. The X-ray powder diffraction patterns were well characterized using Schimadzu Powder X-ray diffractometer at room temperature (Cu-Kα radiation) with nickel filter at a scan rate of 2° min^{-1}. The PL emission spectra for the synthesized NCO's were recorded using Horiba Flurolog Spectrofluorometer at room temperature. ESR was recorded at room temperature with a Bruker ESP 300 spectrometer using a 100 kHz field modulation. In the model ESR experiments, the samples were progressively heated (ex situ) in air in a micro furnace from room temperature up to 1473 K with a rate 4 K/min.

2.6. Preparation of working electrode for electrochemical studies

The synthesized NCO (ZrCu), graphite powder and silicone oil was blended by hand mixing with a mortar and pestle for preparation of carbon paste. The resulting paste was then introduced from the bottom of a Teflon tube. The electrical connection was established by inserting a copper wire in to the Teflon tube. A fresh electrode surface was generated rapidly by extruding a small plug of the paste with a stainless steel rod and smoothing the resulting surface on wax paper until a smooth shiny glassy surface was observed. The same procedure was adopted to prepare carbon paste electrode (working electrode) for other two NCO's.

2.7. Enhancement of human latent fingerprints using ZrO_2/CuO NCO

The LFPs were collected from the same volunteer by washing hands cleanly with soap. The fingers were pressed gently on the different materials including infiltrating and non infiltrating surfaces at room temperature. To enhance LFPs, the synthesized ZrO_2/CuO NCO's was stained cautiously with a smooth brushing method. The surplus powder was removed gently, smooth motion until a fingerprint was enhanced. The enhanced fingerprints were photographed under 254 nm UV light range by using a Nikon D3100/AF-S Nikkor 50 mm f/2.8G ED lens digital camera.
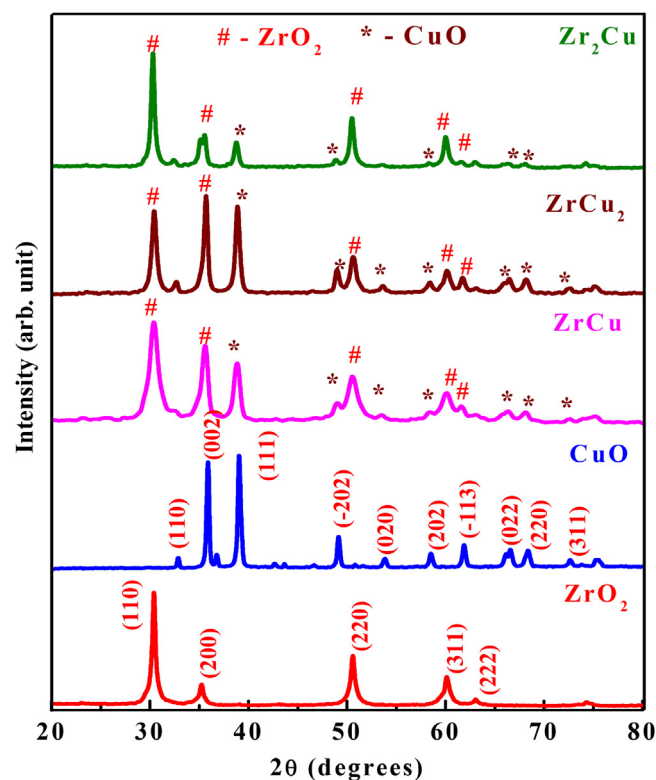

Fig. 1. PXRD patterns of ZrO_2, CuO NPs and ZrO_2/CuO NCO.

2.8. Photocatalytic activity investigation

The required concentration of stock solution of dye was prepared using double distilled water. From the stock solution, required ppm of dye solution was prepared. The indgo carmine (IC) dye solution (20 ppm) and the catalyst (60 mg) was added in a circular glass reactor and exposed to Sunlight. The experiment was carried out under ambient condition in between 12 to 2 pm (month of April, Bangalore) with latitude and longitude of 12.60N and 77.31E respectively. The average solar intensity calculated using solar radiometer was found to be 0.736 kW m^{-2}. The sunlight was concentrated onto a dye solution with photocatalyst by using a convex lens. All the photocatalytic experiment with synthesized samples was carried out simultaneously in order to avoid the error arising due to solar light fluctuations. Before carrying out the experiments, the solution was kept under dark to obtain balance adsorption and desorption equilibration of the system so that the loss of dye due to adsorption can be taken into account. This dye solution is taken in a circular glass reactor and placed under Sunlight after addition of catalyst (ZrO_2, CuO, ZrCu, $ZrCu_2$ and Zr_2Cu). For comparison purpose, under the same experimental condition, photocatalytic activity of commercial P25 was carried out. This suspension was stirred with the help of a magnetic stirrer until the degradation completes. Dye solution (5 ml) was collected at proper time intervals form the circular glass reactor during the illumination time of 60 min. Finally the suspension was centrifuged and analyzed for adsorption of dye before and after illumination to Sunlight under UV–vis spectrophotometer.

3. Results and discussion

3.1. PXRD

Fig. 1 represents the PXRD diffraction patterns of ZrO_2, CuO (NPs) and NCO's (ZrCu, $ZrCu_2$ & Zr_2Cu). Diffraction peaks corre-

sponding to ZrO_2 NPs were clearly observed in the individual as well as in the NCO's patterns. ZrO_2 exists in three phases, namely monoclinic, tetragonal and cubic. Depending upon the methodology, time and temperature, crystallization of ZrO_2 in a particular phase can be identified [47]. The observed planes of pure ZrO_2 were associated with (110), (200), (220), (311) and (222) at $2\theta = 30.30$, 35.40, 50.60, 59.8, and 62.8 respectively with JCPDS card number 27-0997. These planes are then associated with d-spacing values of 2.93, 2.55, 1.80, 1.53 and 1.47 Å, respectively, which can be readily assigned to a cubic phase of ZrO_2 [48]. For CuO NPs, diffraction peaks located at 2θ=32.8, 35.8, 38.8, 49.2, 53.8, 58.7, 62, 66, 68, 72 and 75.4 were associated with (110), (002), (111), (-202),(020), (202), (-113), (022), (220), (311) and (-220) planes respectively with JCPDS card number 80–1916 [49]. High crystallanity of the sample is clearly identified from sharp diffraction peaks. It can be concluded from the positions of the peaks that the inclusion of CuO does not form solid solution with ZrO_2 and the samples ZrCu, $ZrCu_2$ and Zr_2Cu can be regarded as composite powders of crystalline ZrO_2 and CuO.

The crystallite size of ZrO_2 and CuO NPs and NCO's were calculated using Debye–Scherrer formula, $d = 0.89\lambda/\beta \cos\theta$, where 'd' is the crystallite size, 0.89, Scherrer's constant, λ, the wavelength of X-rays, θ, the Bragg diffraction angle, β, the full width at half-maximum (FWHM) of the diffraction peak. The average crystallite size of ZrO_2 and CuO NPs were found to be 18.6 and 17.6 nm respectively, which was derived from the FWHM of more intense peaks. The crystallite size of NCO's was found to be in the range of 15–19 nm.

The W–H approach suggested that when the domain effect and lattice micro strain effect were both simultaneously operative, their combined effects gives the final line broadening FWHM which was the sum of grain size and lattice distortion. This relation assumes a negligibly small instrumental contribution compared with the sample-dependent broadening. W–H plots may be expressed in the form [50,51]:

$$\beta \cos\theta = \frac{0.9\lambda}{D'} + 4\varepsilon\sin\theta \qquad (1)$$

Where β (FWHM in radian), ε; the strain developed and D; the grain size. The equation represents a straight line between $4 \sin\theta$ (X-axis) and $\beta \cos\theta$ (Y-axis), the slope of line gives the strain (ε) and intercept (λ/D) of this line on the Y-axis gives grain size (D). The crystallite sizes estimated from W–H plots (Fig. 2) were slightly higher than those calculated by Debye Scherrer's method as depicted in Table 1.

$$\delta = \frac{1}{D^2} \qquad (2)$$

$$SF = \left[\frac{2\pi^2}{45(3\tan\theta)^{1/2}} \right] \qquad (3)$$

The small variation in the values were due to the fact that in Scherrer's formula strain component was assumed to be zero and observed broadening of diffraction peak was considered as a result of reducing grain size only. The other structural parameters; dislocation density (δ), stacking fault and strain were determined using the following relation and the estimated parameters were mentioned in Table 1.

3.2. Fourier transform infrared spectroscopy (FTIR)

FTIR spectra of ZrO_2,CuO NPs and NCO's synthesized by solution combustion route were analyzed in the range 400–4000 cm^{-1} as depicted in Fig. 3. The peaks were observed at 470, 524, 1022, 1114, 1370, 1652, 2930, 3443 cm^{-1} for all the synthesized samples. This analysis was very much helpful to explain the bonding configuration present in the synthesized NPs and NCO. The peak centered
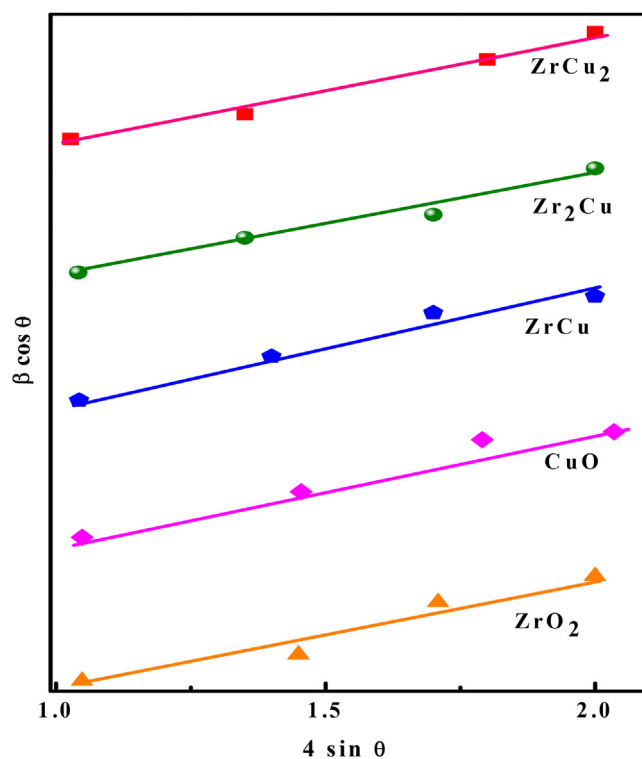

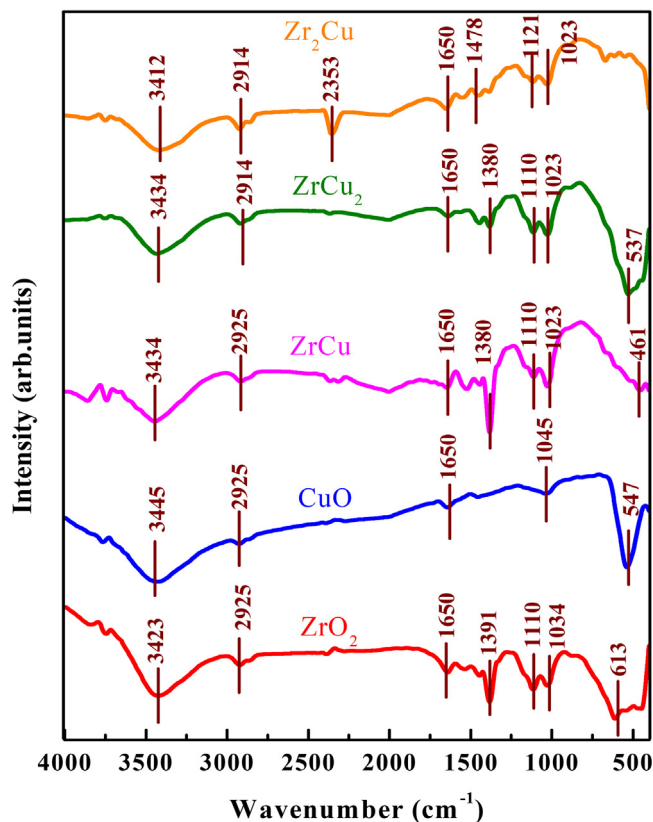**Fig. 2.** W–H plots for ZrO_2, CuONPs and ZrO_2/CuO NCO.

Fig. 3. IR spectrum of ZrO_2, CuO NPs and ZrO_2/CuO NCO.

Table 1
Estimated crystallite size, strain, stacking fault and dislocation density of ZrO_2, CuO NPs and ZrO_2/CuO NCO's.

Samples	FWHM (deg)	Crystalline size (nm)		Strain (e) $\times 10^{-3}$	SF	δ (10^{15} lin m^{-2})
		Scherrer's method	W-H plot			
ZrO_2	0.45	18.6	19.2	2.06	0.4210	2.8
CuO	0.77	17.6	15.5	2.72	0.3885	3.4
ZrCu	0.86	15.5	16	3.52	0.4523	6.5
$ZrCu_2$	0.525	16.4	17.2	2.11	0.4509	3.7
Zr_2Cu	0.44	18.4	19.5	1.87	0.4377	2.9

at $470\,cm^{-1}$ was mainly attributed to Zr—O vibrations [52] that were observed in pure ZrO_2 and Zr_2Cu NCO as zirconia is present more in this sample. The peak at $524\,cm^{-1}$ was attributed to Cu—O vibration [53] in $ZrCu_2$ NCO as the ratio of copper was more in this NCO. The characteristic peak at $1114\,cm^{-1}$ and $1370\,cm^{-1}$ was attributed to C—H bending modes of vibrations. The strongest peak at $1099\,cm^{-1}$ was assigned to the C—O—C bond. It can be seen that there is a distinct absorption band from $1150\,cm^{-1}$ to $1250\,cm^{-1}$, which can be attributed to the C—O—C stretching vibration. The adsorbed band at $1652\,cm^{-1}$ and $1442\,cm^{-1}$ was due to O—H bending and stretching vibrations respectively. The broad peak around $2930\,cm^{-1}$ was ascribed to the stretching vibration of CH_2. Presence of hydroxyl stretching was confirmed from the peak at $3443\,cm^{-1}$, which normally arises due to the moisture content in the synthesized samples.

3.3. Morphological analysis

SEM was predominantly utilized to contemplate the composition, grain, geography and surface components of synthesized samples. The SEM analysis was mainly helpful to provide information about the surface morphology and also about crystalline size. In this investigation, SEM morphologies obtained by solution combustion synthesis for all the synthesized samples were depicted in Fig. 4(a–e).The surface morphology of ZrO_2 NPs consist large number of non-uniform NPs with large number of pores and voids (Fig. 4a). The micrograph of CuO NPs also consists of large number of non-uniform slightly agglomerated NPs (Fig. 4b). Fig. 4(c–e) represents the micrograph corresponding to ZrO_2/CuO NCO's in different ratios. With increase in ZrO_2 or CuO concentration, the particle nature completely disappears and it looks like cloud (Fig. 4c and d). For Zr_2Cu along with cloud appearance, slight agglomeration is observed (Fig. 4e). Here, as Zr_2Cu contains more number of pores, it may allow multiple light reflections with more absorption of light resulting in higher photocatalytic activity.

The TEM image indicates the presence of irregular shaped crystals among them few are larger in size and maximum numbers of the crystals are smaller in size. Fig. 5 shows the TEM, HRTEM images, SAED and EDX pattern of Zr_2Cu NCO. The careful observation says the random distribution of the larger sized NPs smoothly on the surface of smaller sized NPs (Fig. 5a and b). The as-acquired SAED pattern is well – indexed by characteristic d-spacing for both ZrO_2 and CuO confirming the distribution of CuO crystallites all over the ZrO_2 lattice matrix as represented in Fig. 5e. Interfacial bonding between CuO NPs with ZrO_2 matrix is depicted in High resolution (HRTEM) image (Fig. 5c &d). The EDX spectrum (Fig. 5f) shows the presence of Zr, O and Cu elements. The average crystallite size estimated for Zr_2Cu was in good agreement with the size estimated by Scherrer's equation from PXRD pattern. Combining with PXRD analysis above, these results further confirm that CuO effectively built into the ZrO_2 host lattice.

Further, for a clear comprehension of the interfacial bonding between CuO NPs and ZrO_2 matrix, HRTEM images have been depicted in Fig. 6(a–d). In order to visualize the lattice fringes of the structure, a particular region of Fig. 6a (upper right) with three distinctive regions (region 1–3) have been selected. With interplanar spacing of about 0.3218, the atomic layers illustrate apparent and continuous lattice fringes which is associated with the (110) lattice spacing of ZrO_2 matrix as observed in Fig. 6b (region 1). With further observation in the region 2 (Fig. 6c), the structure of CuO with interplanar spacing of 0.2526 nm is due to the (111) plane of orientation of lattice was distinctly revealed. Beyond this region, Fig. 6d shows two sets of lattice fringes that $d_{110} = 0.3218$ nm of ZrO_2 and $d_{111} = 0.2526$ nm of CuO proves the ZrO_2—CuO interface (region 3). At the ZrO_2/CuO interface, atomic arrangement is disoriented and this could be of the lattice mismatch as a result of introduction of novel chemical compound such as CuO into ZrO_2 during the stages of synthesis. Studies have demonstrated that this may be due to the hetero-junction interfacial materials that are made up of two different compounds [54,55]. Due to the defects found in the atomic levels, lattice mismatching and disorientation may happen. This defect is commonly associated with the different chemical potential of the secondary compound which gives rise to a newly ordered crystalline structure by adjusting the lattice spacing and hence lattice rearrangement takes place. With respect to all these structural analysis results, it is proved this synthesis procedure has successfully incorporated CuO NPs into the ZrO_2 lattice matrix by means of solution combustion method.

3.4. N_2 adsorption-desorption isotherm

N_2 adsorption-desorption isotherms were applied to investigate the porous structure and surface area for the synthesized NCO's. All the synthesized NCO's were preheated at $100\,°C$ for 1 h before N_2 adsorption. A small hysteresis loop with high relative pressure region (>0.9 P/P_0) indicates the macroporosity of the obtained ZrCu NCO. The mesoporous nature of $ZrCu_2$ and Zr_2Cu NCO's is proved by the irreversible type IV adsorption/desorption isotherm [56,57]. As shown in Supplementary Fig. S3, the surface area of the synthesized NCO's ZrCu, $ZrCu_2$ and Zr_2Cu was found to be 6.09, 25.7 and 15.2 m^2/gm respectively. According to Weimin Du et. al., some nanomaterials may possess higher surface area but its photocatalytic activity was found to be poor. Hence, the surface area was not only the decisive factor deciding the photocatalytic activity [58]. As mentioned above, in the present study NCO $ZrCu_2$ has maximum surface area but in contrary its photocatalytic activity was found to be poor compared to Zr_2Cu.

3.5. Electron paramagnetic resonance (**EPR) analysis**

Many kinds of point defects are present in solids and in particular, oxides are paramagnetic. EPR spectroscopy is one of the most suitable techniques to investigate defective materials. As it will be shown in this section, the behaviour of all the NCO materials examined is basically the same except for the spectral intensity which is slightly lower in the case of Zr_2Cu NCO indicating that the nature and properties of defects are substantially the same as depicted in Fig. 7. The EPR spectrum of ZrCu and $ZrCu_2$ consists two distinct signals I and II. In each case the detected signal was attributed to Zr^{3+}. Among them the Signal I (appeared in the lower magnetic
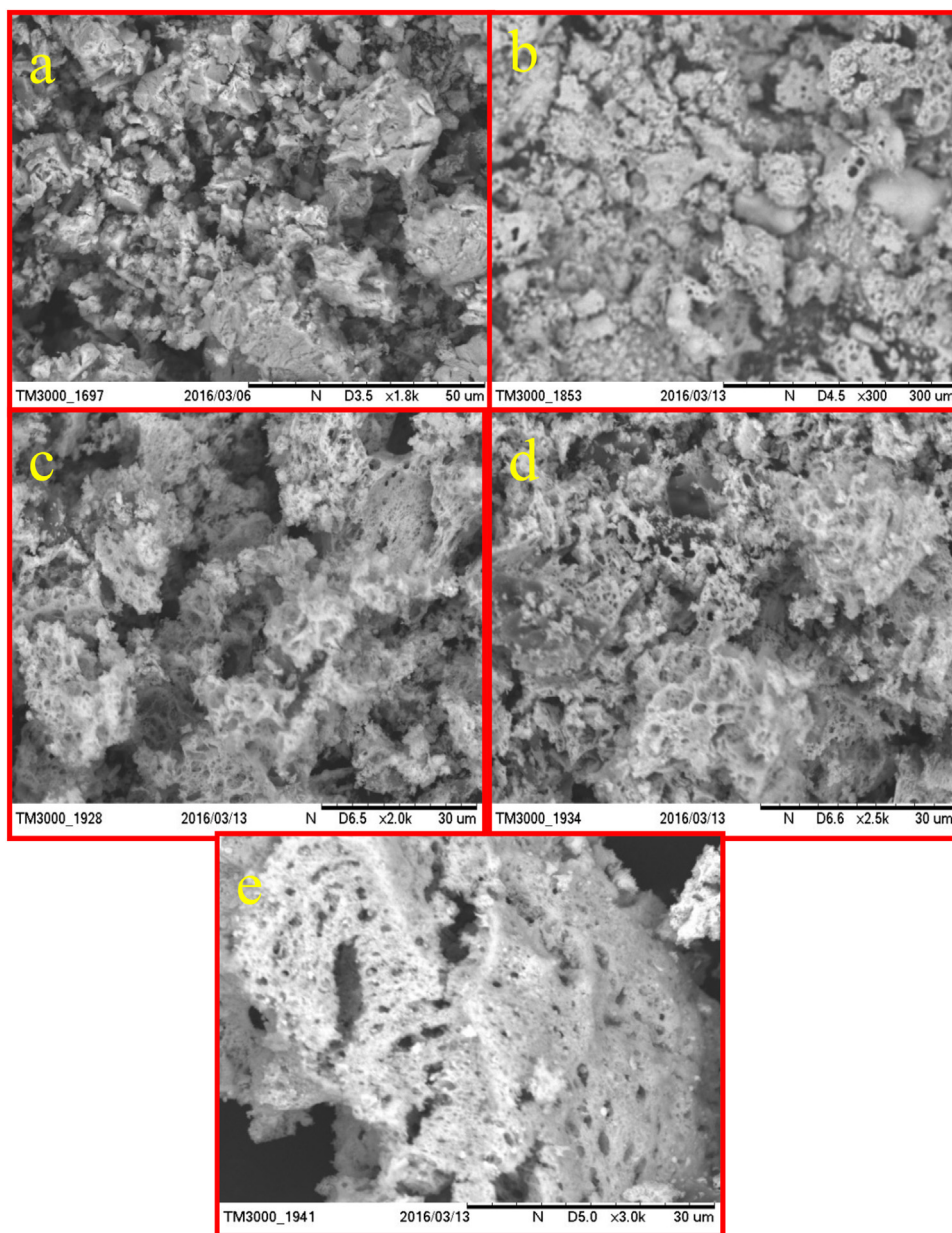
Fig. 4. SEM images of **(a)** ZrO_2 **(b)** CuO NPs **(c)** ZrCu **(d)** $ZrCu_2$ **(e)** Zr_2Cu NCO.

field region) is weak whereas the Signal II (appeared in the higher magnetic field region) is strong. However, one piece of evidence suggests that these centers are at or near the surface rather than within the bulk [59]. The Signal I is totally absent in Zr_2Cu NCO probably due to the formation of more stable defects [60].

3.6. X-ray photoelectron spectroscopy (XPS)

The XPS analysis has been performed to estimate the surface composition and chemical states of the Cu, Zr, and O elements in Zr_2Cu NCO. The wide scan spectra in Fig. 8a demonstrates that the binding energy peaks at 184.2, 287.5, 531.0 and 934.9 eV can be attributed to Zr 3d, C 1s, O1s and Cu 2p respectively. In high resolution Zr 3d spectra (Fig. 8b), the binding energies at 182.0 and 184.2 eV indicates the presence of Zr $3d_{5/2}$ and Zr $3d_{3/2}$ respectively associated with Zr^{4+} matching well with available data for ZrO_2 [61]. The peak at 529.5 eV is a proof of presence of O 1s in Zr_2Cu NCO (Fig. 8c). The Cu 2p peak of the NCO is shown in Fig. 8d.

The Cu $2p_{3/2}$ is allocated at 934.2 eV with a shakeup satellite peak at about 942.5 eV, which is in agreement with previous researches [62,63]. The presence of shakeup satellite features for Cu 2p rules out the chances for the presence of Cu_2O phase.

3.7. UV–vis diffuse reflectance studies

UV–vis diffuse reflectance spectroscopy is used to portray the optical absorption and also energy band gap for the synthesized ZrO_2, CuO NPs and ZrO_2/CuO NCO's. Fig. 9a represents the graph plotted between reflectance and wavelength for the synthesized NCO's. From the figure, it is clear that the absorbance for synthesized NCO's decreases as the CuO ratio decreases. As the wavelength decreases, the absorbance value also decreases.

The absorption co-efficient near the fundamental edge always depends on phonon energy in case of semiconductors. Thus tauc's equation was very much helpful to find out the optical absorption depending on phonon energy for the synthesized NCO's [64]. In
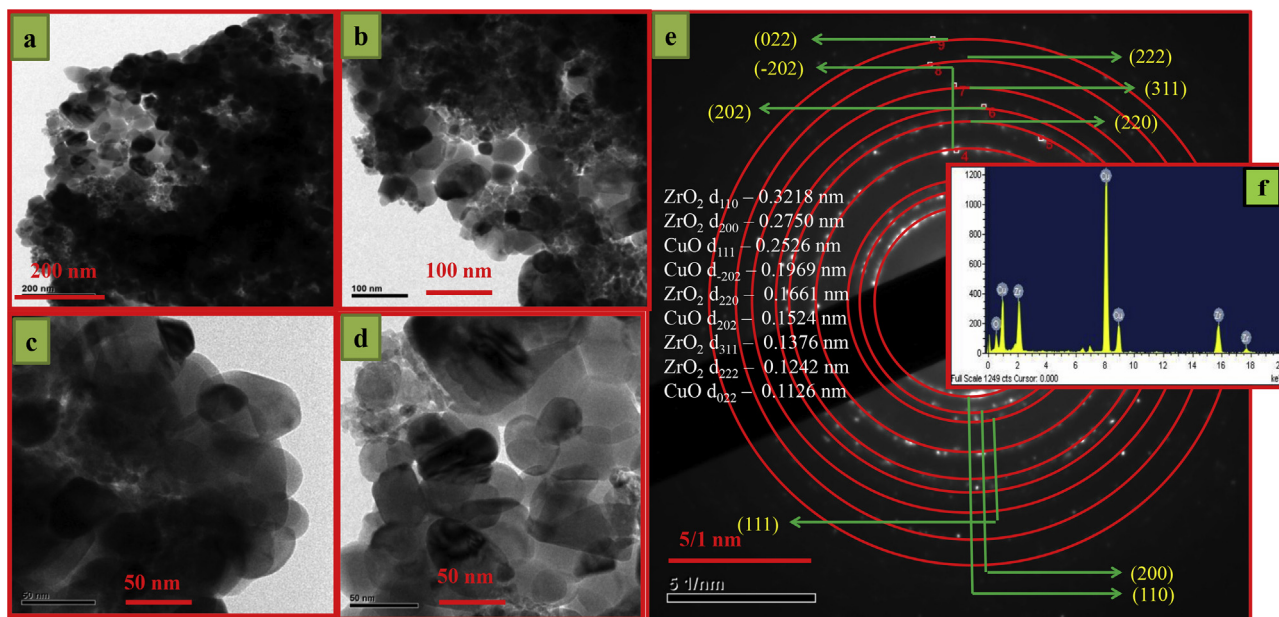
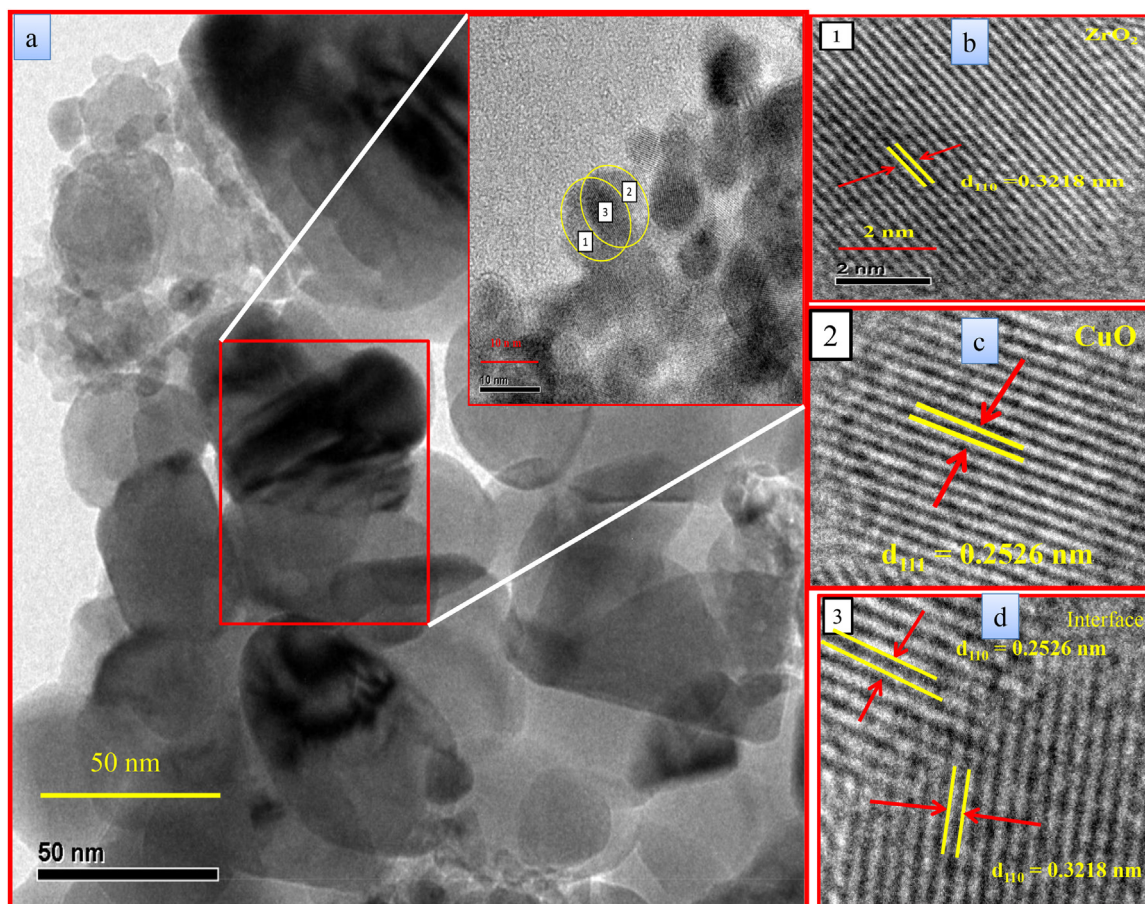**Fig. 5.** TEM images (a & b), HRTEM images (c and d) and SAED (e) with EDX pattern (inset of f) of Zr_2Cu NCO.

ZrO_2 d_{110} − 0.3218 nm
ZrO_2 d_{200} − 0.2750 nm
CuO d_{111} − 0.2526 nm
CuO d_{-202} − 0.1969 nm
ZrO_2 d_{220} − 0.1661 nm
CuO d_{202} − 0.1524 nm
ZrO_2 d_{311} − 0.1376 nm
ZrO_2 d_{222} − 0.1242 nm
CuO d_{022} − 0.1126 nm

Fig. 6. (a) HRTEM image of Zr_2Cu nanocomposite (inset of (a)) The magnified region showing the interface of a typical ZrO_2 and CuO NPs, (b–d) represent the high magnification of HR-TEM images corresponding to ZrO_2 (1), CuO (2) and interface (3) region.

order to calculate the energy band gap, given Tauc's relation was used.

$$\alpha h\upsilon = A(h\upsilon - E_g)^n \qquad (4)$$

where α is the absorption coefficient, h is Planck's constant, υ is the frequency of incident photon, A is the constant depending on transition probability, E_g is the optical band gap energy and n is an index which depends on the nature of electronic transition. Tauc's
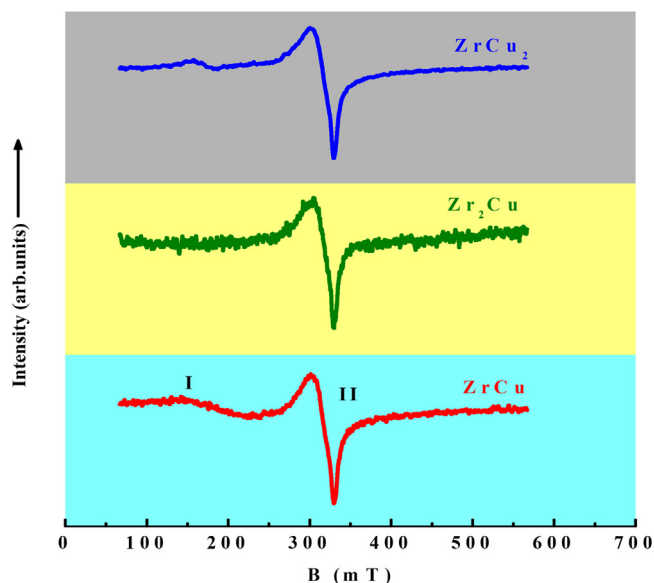
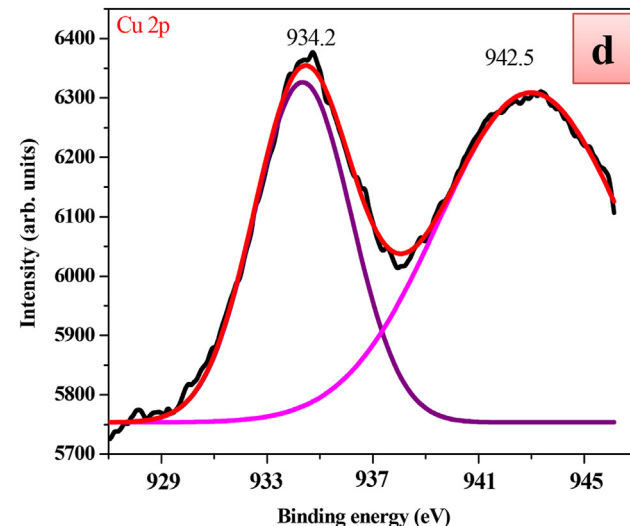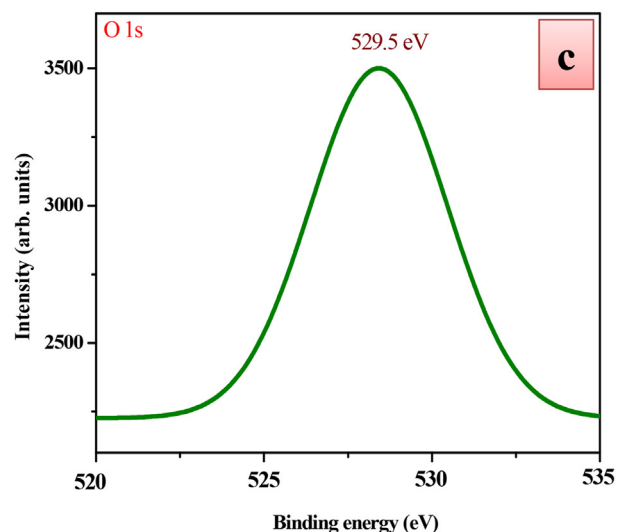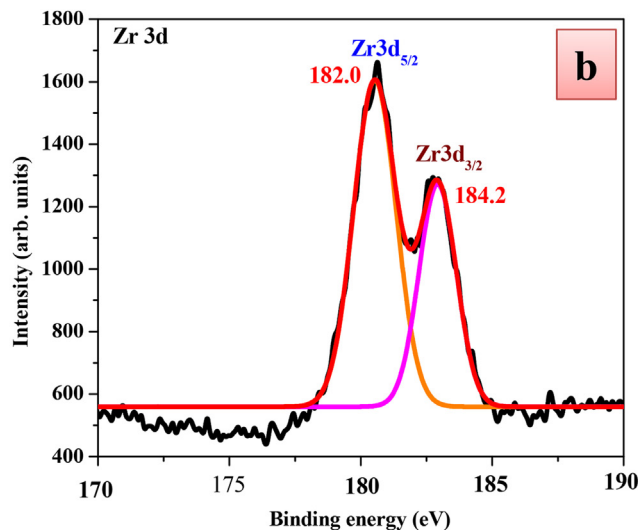**Fig. 7.** EPR spectrum of ZrCu, ZrCu₂ & Zr₂Cu NCO.

plot was helpful to determine the energy band gap at room temperature. By extrapolation the linear part of X-intercept to $(\alpha h\upsilon)^2 = 0$, gives direct energy band gap for synthesized samples. The energy band gap of ZrO_2 and CuO NPs were found to be 5.1 and 1.9 eV respectively as shown in Fig. 9(b & c).The energy band gap values were found to decrease as the ratio of CuO in NCO's decreases as shown in Fig. 9d. The Zr_2Cu NCO was found to have less energy band gap of 1.9 eV. This decrease in the band gap for NCO ($ZrCu$, $ZrCu_2$, Zr_2Cu) compared to ZrO_2 and CuO NPs was mainly attributed to the inclusion of CuO into ZrO_2 matrix, that makes the band gap to decrease rapidly and also due to the change in their crystalline size. The variation of energy band gap with respect to crystalline size was depicted in Fig. 9e. It was found that when two metals are combined, the energy band gap was found to decrease and hence red shift was observed. The energy band gap was found to be less for ZrO_2/CuO NCO compared to pure ZrO_2 and the same results was analogous for other composite studies also [65,66].

The conduction band (CB) and valence band (VB) edges were used to recognize the variation in band gap for synthesized samples. The following equation has been used to determine the CB and VB values.

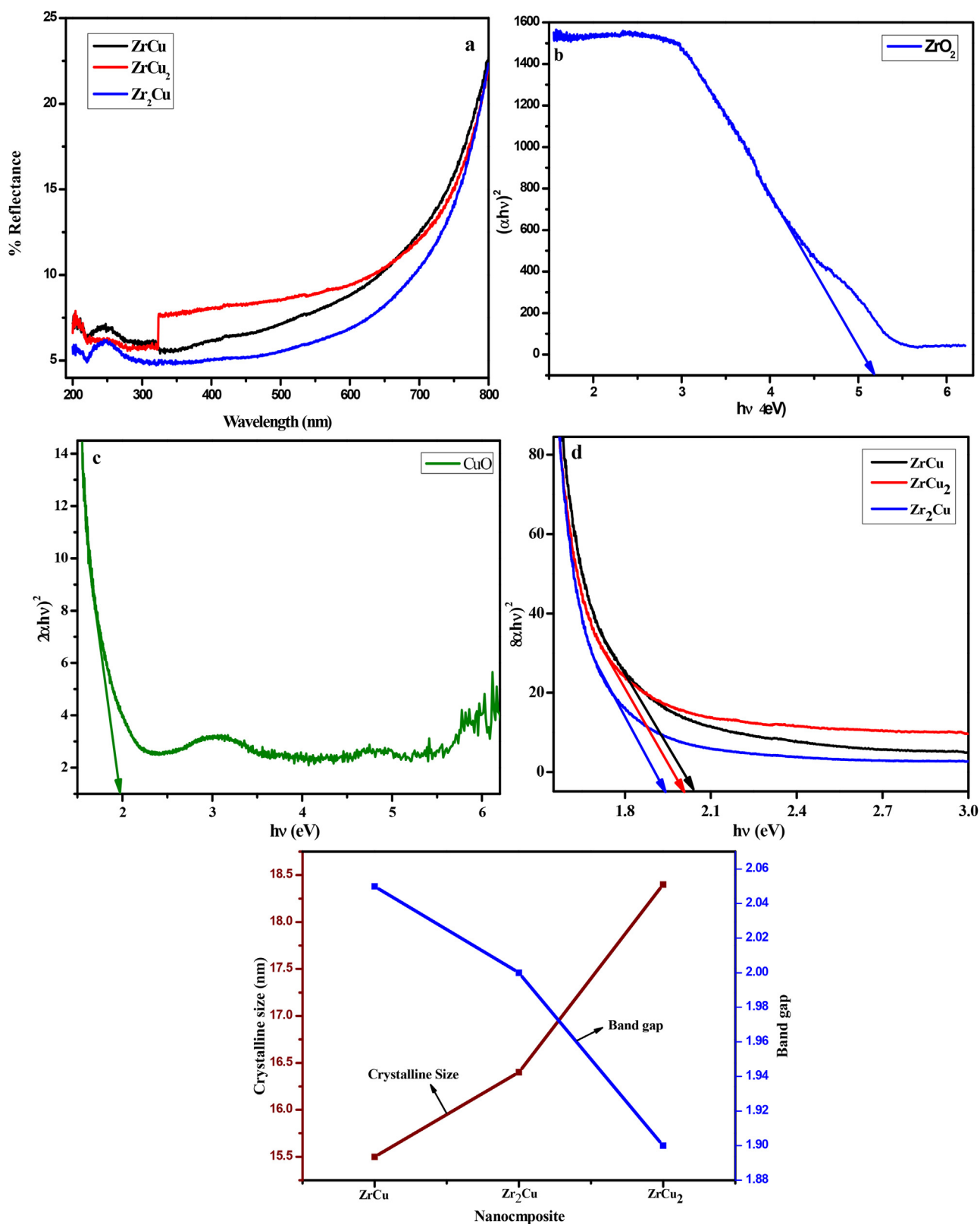$$E_{cb} = X - E^c - 0.5E_g \qquad (5)$$

Fig. 8. XPS spectra of ZrO_2/CuO NCO **(a)** survey spectrum **(b)** Zr 3d **(c)** O 1 s **(d) Cu 2p** peaks.

Fig. 9. (**a**) % Reflectance Vs wavelength of ZrO_2/CuO (**b**) Wood and Tauc's plot to find band gap for ZrO_2 NPs (**c**) Wood and Tauc's plot to find band gap for CuO NPs (**d**) Wood and Tauc's plot to find band gap and the variation in band gap of ZrO_2/CuO NCO (**e**) Variation of band gap with respect to crystalline size for synthesized ZrO_2/CuO NCO.

where E_{CB} is the CB edge potential; X is the electronegativity of the semiconductor, which is the geometric mean of the electronegativity of the constituent atoms, E^c is the energy of free electrons on the hydrogen scale (4.5 eV); and E_g is the band gap energy of the semiconductor. The E_{VB} value was obtained using the following equation
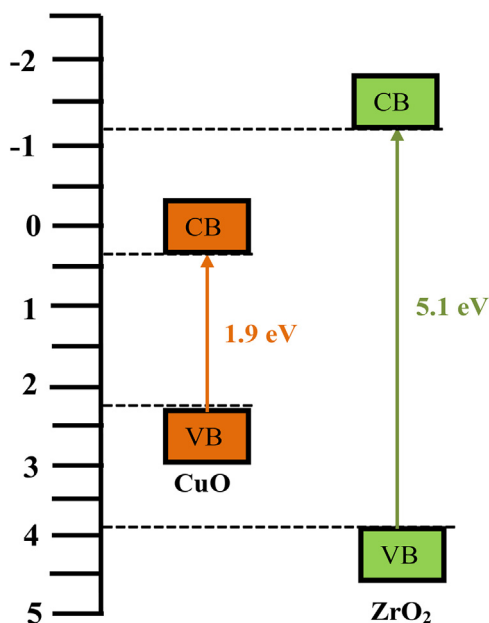
$$E_{vb} = X - E^c + 0.5E_g \tag{6}$$

Fig. 10. Band structure of ZrO_2 and CuO NPs.

Using above relation, the calculated CB values of ZrO_2 and CuO NPs were found to be -1.14 and 0.4 respectively, while the VB values were of 3.96 and 2.3 eV respectively (Fig. 10). The absolute electronegativity for ZrO_2 and CuO was found to be 5.9 and 5.81 respectively [67]. Electrons were excited from VB to CB leaving behind the same number of holes in the VB, when the NCO was subjected to Sunlight illumination. As there was less energy band gap, the electrons can easily transfer from CB of ZrO_2 to CB of CuO. In the meanwhile, holes on the VB of CuO will migrate to VB of ZrO_2 and thus inhibiting the recombination and increase the lifetime of photo-generated electrons and holes, hence enhancement in the photocatalytic activity of the corresponding NCO may be expected.

3.8. Electrochemical studies

3.8.1. Cyclic voltammetry (CV)

The electrochemical characteristics and super capacitive nature of the synthesized NCO's were analyzed by using CV plot with the help of prepared carbon paste electrode. Here the experiment was carried out with conventional three electrode setup by choosing Ag/AgCl as reference electrode, platinum electrode as counter electrode and the prepared carbon paste electrode with synthesized NCO's ($ZrCu$, $ZrCu_2$, Zr_2Cu) will act as a working electrode. The CV experiments were carried out by using 0.1 M $NaNO_3$ as electrolyte in the potential window 1.0 to -0.4 V at the range of scan rate of 50 mV/s and the results were revealed in Fig. 11a. The synthesized NCO's contains rectangular shape as represented for double layer capacitance. But the shape of $ZrCu_2$ and Zr_2Cu was not found to be deviated from rectangle shape [68]. The capacitances of the synthesized NCO's follow the order: $Zr_2Cu > ZrCu_2 > ZrCu$.

3.8.2. Electrochemical impedance spectroscopy (EIS)

EIS is a widely used electrochemical method in order to explore the electron transfer process across electrode and electrolyte interface along with charge transfer resistance values [69]. EIS was carried out by choosing 0.1 M $NaNO_3$ solution as electrolyte. It is well known that photocatalytic studies can be explained clearly with the help of impedance in electrochemical studies.

EIS measurements were performed on synthesized NCO's in order to determine the best NCO for good charge separation, as
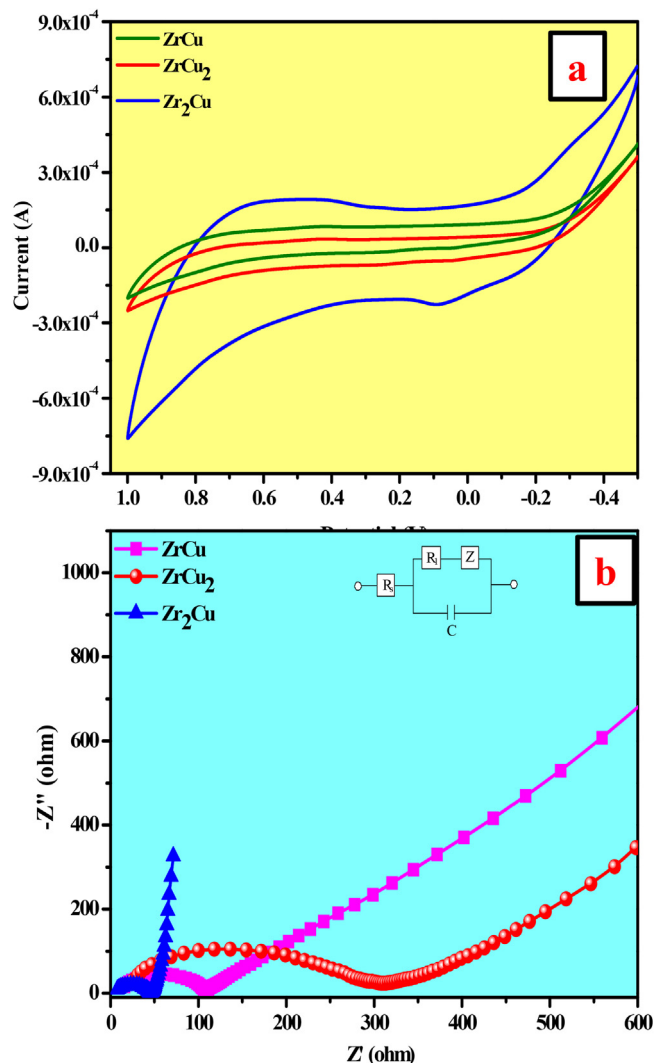

Fig. 11. (a) CV plots for ZrO_2/CuO NCO at scan rate of 50 mV/s (**b**) Nyquist plot for ZrO_2/CuO NCO.
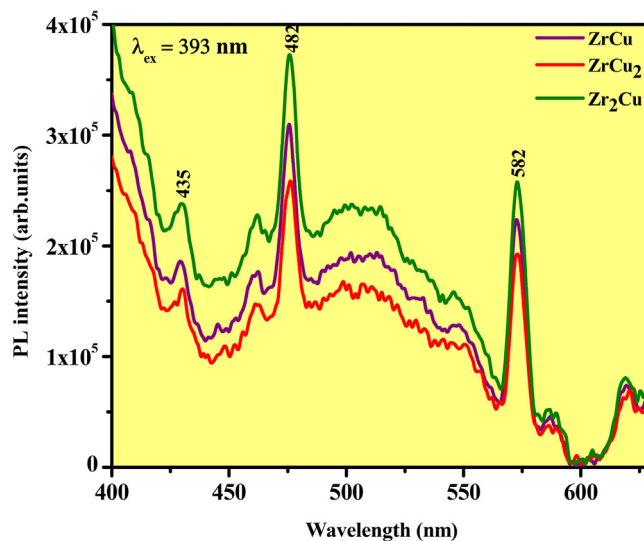

Fig. 12. PL emission spectrum of ZrO_2/CuO NCO excited at 393 nm.

shown in Fig. 11b. Usually the semicircle represents the high frequency range which may be due to the charge transfer resistance and linear line represents the low frequency range which attributes to Warburg impedance (W). Further, the linear line for Zr_2Cu leans more towards the vertical Z" axis indicating that the sample has a better capacitive performance. The radius of semicircle represents the interface layer resistance that takes place at the surface of the electrode. The obtained values of charge transfer resistance for NCO's ZrCu, $ZrCu_2$ and Zr_2Cu was found to be 98, 290 and 50 Ω respectively. Thus out of these values mentioned above, Zr_2Cu NCO has got smaller semicircle. This decrease in the radius of semicircle is ascribed to the following reasons such as at the electrode–electrolyte interface the depletion layer shrinks, hence decreases the resistance offered by the film-electrolyte interface. Due to this, diffusion of ions into pores of electrode will be slowed down rapidly. Thus Zr_2Cu has smaller semicircle with higher charge transfer resistance indicating high charge transfer rate hence enhanced photocatalytic activity.

A reasonable equivalent circuit for Zr_2Cu NCO with high photocatalytic activity from the obtained impedance studies has been proposed (Inset Fig. 11b) to fit the experimental data, which can be explained as following: First, series and parallel combination of solution resistance (Rs), electrolyte resistance (R_1) present in the pores and double layer capacitance (C_{dl}) that helps to create semicircle at high frequency in the impedance spectra. Second, the line represented by Warburg impedance (Z) having phase angle of 45° indicating the transport of ions into the bulk of electrode [70].

3.9. Photoluminescence (PL) spectroscopy

ZrO_2 contains only Zr—O bonds that do not have luminescence property. An electronic state is introduced into the band gap when there is transformation of phase and the presence of structural defects in different phases which results in luminescence of these materials [71]. To define ZrO_2 luminescence, three kinds of luminescence had been explained [72,73]; (a) from an impurity/dopant (b) intrinsic self trapped excitons (c) from intrinsic defects – (F and F^+ centers, Zr^{3+}). Solution combustion process results in the presence of large number of surface defects (oxygen vacancy or interstitial oxygen, Zr vacancy or Zr interstitial) in ZrO_2 due to their large surface area of nano-sized particles [74]. According to Kroger's notation, the formation of oxygen vacancies can be explained by the following equations (7a–7d).

$$ZrO_2 \leftrightarrow ZrO_{2-n} + \frac{n}{2}O_2(g) \tag{7a}$$

$$O_o{}^* \leftrightarrow \frac{1}{2}O_2(g) + V_o \tag{7b}$$

$$V_o \leftrightarrow V_o{}^* + e^- \tag{7c}$$

$$V_o{}^* \leftrightarrow V_o{}^{**} + e^- \tag{7d}$$

Where V_o, $V_o{}^*$, $V_o{}^{**}$, $O_o{}^*$ and e^- corresponds to a neutral oxygen vacancy, a singly ionized oxygen vacancy, a doubly ionized oxygen vacancy, an oxide ion in a regular lattice site and the presence of an electron in conduction band respectively.

With an excited wavelength centered at 393 nm, the photoluminescence emission spectra were recorded. Fig. 12 depicts the room temperature PL spectra of synthesized NCO's. Upon excitation, a sharp violet emission with less intensity centered at 435 nm, sharp high intense blue and green emissions centered at 482 and 582 nm was observed. It is found that the PL excitation band around 393 nm can be attributed to defect states due to oxygen vacancies that exist at the grain boundaries. Anion vacancies are the principal intrinsic defects in nano-crystalline zirconia. This could be implicated to the formation of electrons (F and F^+ centers) [75]. The emission is attained by this singly ionized oxygen that results from the

radiative recombination of a photo-generated hole with an electron occupying the oxygen vacancy. The PL emission bands in the violet region may be due to the transitions from the surface trap states in the conduction band to lower levels of energy closer to the valance band. The high intensity band centered at 482 nm emission may be due to the presence of oxygen vacancies. Because of the uniform nature of the size and shape of the particles obtained through the solution combustion, high quality nanophosphors and sharp emission may be observed. D. Manoharan et al., also reported such unique sharp emission in Zirconia is highly preferable for sophisticated optical applications [72]. Also, it could be considered that the multiple emission of violet, blue and green light on exciting the NCO is the distinctive property of the solution combustion synthesized samples.

As already explained, these emissions occur mainly due to oxygen vacancies and surface defects [76]. Therefore stronger PL signal occurs easily as defects and vacancies are more in the NCO's. As the vacancies are more, it will be helpful to increase the oxygen adsorption and capture photo-induced electrons forming oxygen radical finally. This oxygen radical and defects has a vital part in enhancing the photocatalysis by degrading the dye. The emission peak at 582 nm mainly arises due to the contribution of mid-gap trap states like surface defects.

It is discussed by Liqiang and his co-workers that smaller photoluminescence intensity due to lower recombination causes higher photocatalytic activity of semiconductor. But this is not true in all the cases. Sometimes, when there is increase in surface defect and oxygen vacancies at the surface, there will be higher intensity of photoluminescence and photocatalytic activity [77]. Solution combustion synthesized NCO's contains pores due to which more amounts of defects and vacancies are produced. As shown in Fig. 12, the PL intensity for Zr_2Cu NCO was found to be high due to the large number of oxygen vacancies and surface defects compared to ZrCu and $ZrCu_2$ NCO's. Hence Zr_2Cu NCO has high PL intensity and high photocatalytic activity as already explained by Damian Wojcieszak and co-workers [78].

Using De Mello [79] and Palsson [80] method, the quantum efficiency (QE) of the optimized ZrO_2/CuO can be determined.

$$QE = \frac{Number\,of\,photons\,emitted}{Number\,of\,photons\,absorbed} = \frac{E_c - E_a}{L_a - L_c} \tag{8}$$

Where, E_C is the phosphor integrated luminescence from direct excitation, E_a is the integrated luminescence from the vacant integrating sphere (blank without sample), L_a is the integrated excitation profile from the vacant integrating sphere, L_C is the integrated excitation profile when the sample is directly excited by the incident beam. The QE for the ZrO_2/CuO nanophosphor excited at 393 nm was estimated to be ∼64% by integrated emission counts suggest the high QE of the synthesized sample. On the other hand, in our previous research studies the QE was found to be 61% for $GdAlO_3:Eu^{3+}$ [81].

Room temperature PL spectra can be used to estimate the Commission Internationale de I'Eclairage (CIE 1931) chromaticity coordinates and the corresponding CCT of the blue emission in the present NCO's. The resulting CIE diagram is shown in Fig. 13a. It can be seen from the CIE diagram that the chosen NCO slightly moves from (0.232, 0.30414) to (0.22684, 0.29408) describing the blue light emission as shown in inset of Fig. 13a. The quality of the blue light by using McCamy empirical formula [82] in terms of correlate color temperature (CCT) values were found to be 14124, 13551, 15948 K for NCO (ZrCu, $ZrCu_2$, Zr_2Cu) respectively (Inset Fig. 13b). These CCT values lie in the warm blue region (see Fig. 13b). Thus, the prepared NCO's exhibits the characteristic warm blue light emission
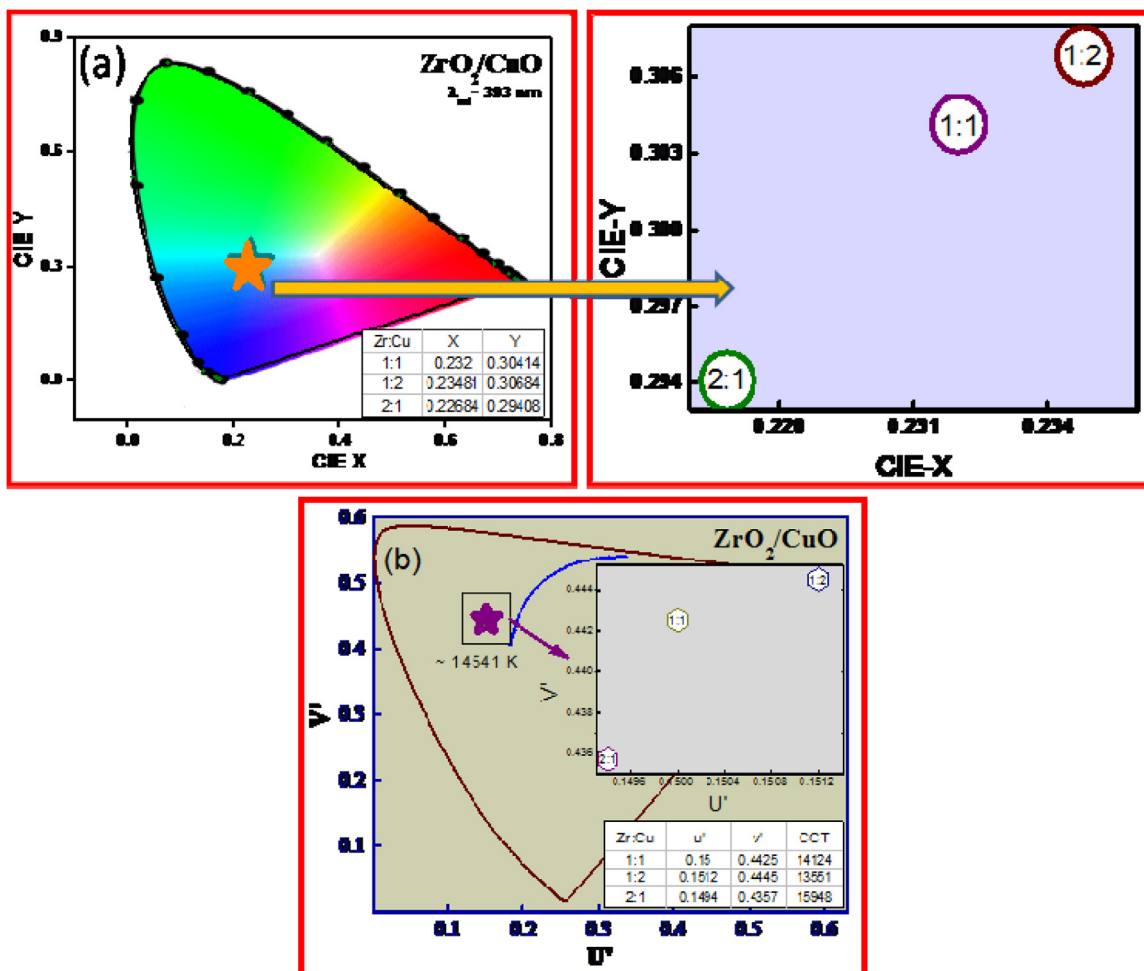
Fig. 13. (a) CIE chromaticity diagram of ZrO_2/CuO NCO (Inset: CIE chromaticity coordinates of ZrO_2/CuO NCO) (b) CCT diagram of ZrO_2/CuO NCO (Inset: CCT values).
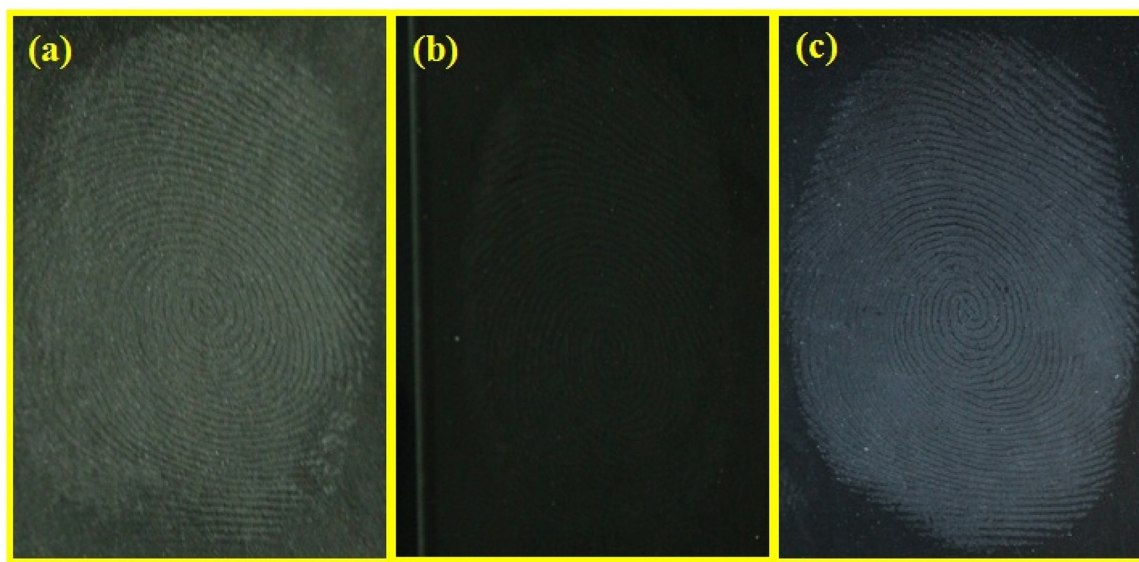

Fig. 14. Comparison of the LFPs stained by (a) TiO_2 powder, (b) magnetic powder and (c) Zr_2Cu NCO material.

3.10. LFPs detection

Zr_2Cu NC comparatively showed higher photocatalytic and photoluminescence activity than that of ZrCu and $ZrCu_2$. Hence, Zr_2Cu NCO could be preferably experimented towards fingerprint analysis. To compare the sensitivity and efficiency of the synthesized Zr_2Cu NCO, traditional labeling powders were used as controls. The LFP images developed by commercial magnetic powder (Fe_3O_4),
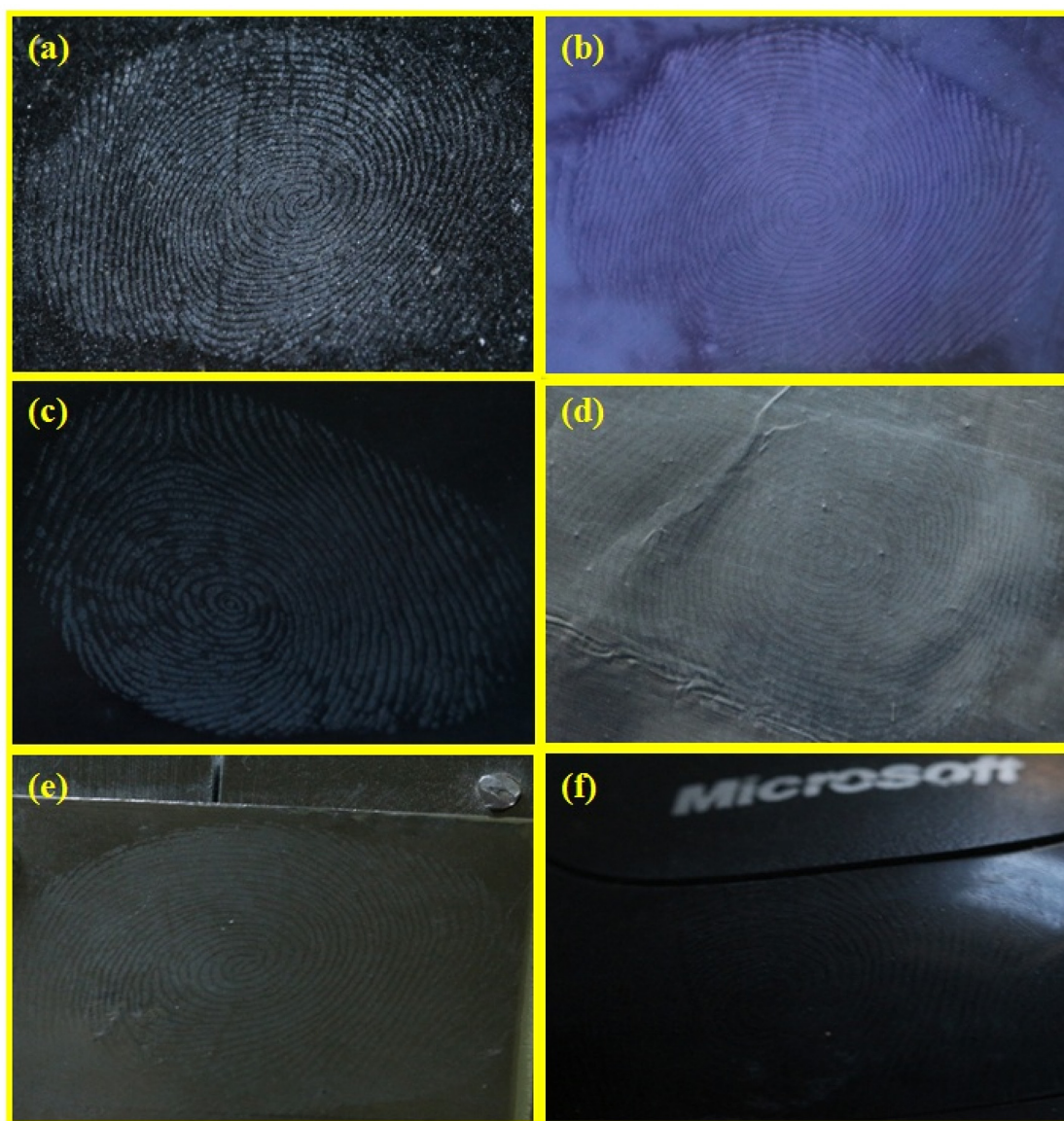
Fig. 15. LFPs under UV 254 nm enhanced by Zr_2Cu NCO on: (a) marble, (b) compact disk, (c) glass, (d) aluminium foils (e), stainless steel and (f) computer mouse.

Commercial TiO_2 and synthesized Zr_2Cu NCO on a glass slide under UV light (254 nm) were shown in Fig. 14(a–c). Under UV light, fingerprints developed by conventional powders could not be clearly determined. As compared to commercial powders, fingerprint stained by Zr_2Cu NCO effortlessly enhances LFPs with clearer minutiae ridges due to their smaller crystalline size (Fig. 14c). Hence, it was substantiating that, synthesized Zr_2Cu NCO was quite useful in order to enhance latent LFPs in different porous and non-porous materials.

The enhancement of LFPs on different smooth non-infiltrating materials surfaces such as marble, compact disc, glass, aluminium foil, stainless steel and computer mouse stained by fabricated ZrO_2/CuO NCO under UV light was investigated as shown in Fig. 15(a–f). It was evident that the well-defined minutiae ridge patterns were identified without any color hindrance under UV light, signifying that enhancement of LFPs by powder dusting method with Zr_2Cu NCO. Thus the synthesized Zr_2Cu NCO was used as functional labeling material to reveal LFPs on forensic relevant non-filtrating surfaces.

Usually, the enhancement of LFPs on infiltrating materials was practically quite difficult for developer due to absorption of the constituents of LFPs by these materials. The LFPs on different papers stained by fabricated Zr_2Cu NCO enhances fingerprints without any background interference (Fig. 16(a–d)). This holds the versatility of the fabricated NCO sample for enhancement of LFPs for forensic analysis.

Fig. 17 shows the digital photographs of LFPs stained by Zr_2Cu NCO. The enhanced fingerprint displays a well-resolved ridge flow and pattern configuration with clear resolution between bright ridge and dark substrate (level 1). In addition to level 1 details, level 2 (ridge termination, bifurcation, crossover and etc) characteristics of the LFP are also clearly observed, which is critical for identification of individuals.

Pictorial representation of the enhancement of LFPs using Zr_2Cu NCO photocatalyst by dusting process and also SEM image of Zr_2Cu NCO for clear observation of fingerprint ridges and particle distribution in ridges has been depicted in Fig. 18. Fingerprints developed by Zr_2Cu NCO show patterns with high efficiency (because procedure involves simple experimental setup and rapid formation
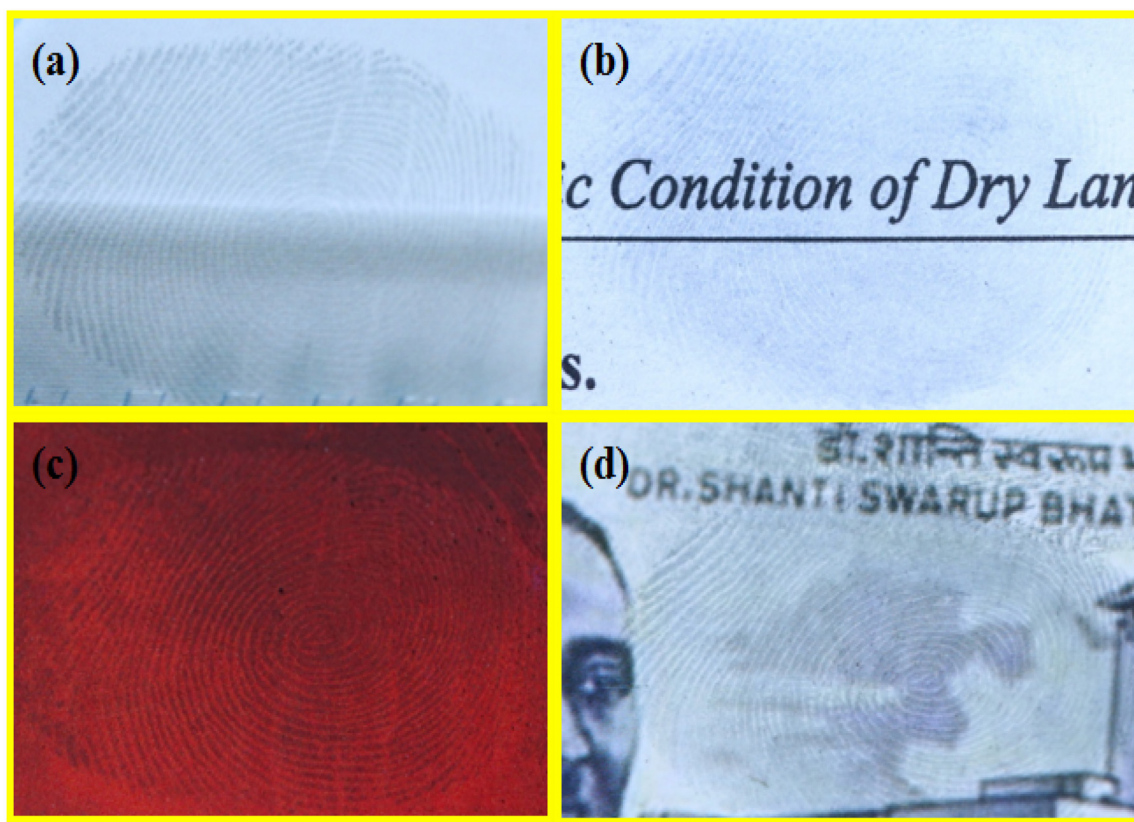
Fig. 16. LFPs on the surface of various paper, which were stained by ZrO$_2$/CuO NCO material with different background color.

of products within 5 min) and high sensitivity (because no color interference and chemical constituents can be observed due to nano size). We successfully demonstrated the fabricated Zr$_2$Cu NCO employed as a labeling agent to enhance LFPs on different surfaces.

3.11. Photocatalytic experiments

3.11.1. Effect of catalyst dosage

With fixed IC dye concentration, the amount of catalyst added was analyzed. The catalyst dosage was varied from 20 to 100 mg for 250 ml of dye solution. The degradation was observed to be high when the catalyst dosage was 60 mg. The reason for maximum degradation of 97% at this catalyst dosage is attributed to presence of more number of active sites which in turn increases the adsorption of dye molecules. When the catalyst dosage was increased above 60 mg, the dosage was found to be high which results in decrease in percentage of degradation from 97 to 60%. Hence, a higher amount of catalyst dosage leads to turbidity on the solution that reduces the penetration of light.

3.11.2. Effect of dye dosage

The effect of dye solution also plays a very important role in photocatalysis. The catalyst dosage was fixed constant by changing the dye concentration. The dye concentration was varied from 20 to 100 ppm. The percentage of degradation was found to be high when the concentration was less. 20 ppm dye solution showed higher degradation compared to other concentrations chosen. When the concentration of dye solution increases, the light can penetrate less into the solution that leads to lesser degradation of the dye solution.

3.11.3. Catalyst performance

By optimizing the amount of dye solution (20 ppm) and catalyst dosage (20 mg) to be added, the photocatalytic experiment was car-ried out for all the synthesized NCO's and compared with the pure ZrO$_2$ and CuO NPs for degradation of IC dye solution under Sunlight illumination. The dye solution was exposed to dark condition without adding catalyst and the degradation percentage was found to be negligible. For comparison purpose, a controlled experiment was carried out without addition of catalyst. The degradation of synthesized NCO was found to be higher compared to pure ZrO$_2$ and CuO NPs as represented in Fig. 19b. Zr$_2$Cu photocatalyst showed enhanced photocatalytic activity of 97% compared to other photocatalysts. It is observed that as the ratio of zirconia increases, the photocatalytic activity also increases. The order of photocatalytic degradation of IC dye along with degradation percentage was as follows: Zr$_2$Cu (97) > ZrCu$_2$ (85) > ZrCu (80) > commercial P25 (65.2) > ZrO$_2$ (30) > CuO (40). It can be concluded that compared to commercial P25, Zr$_2$Cu NCO photocatalyst exhibits higher photocatalytic activity for the degradation of IC dye under the same experimental condition [83].

The increase in the photocatalytic activity of Zr$_2$Cu was mainly due to the presence of more number of oxygen vacancies and surface defects (PL), narrow band gap (DRS) and less crystalline size (PXRD). This result obtained for photocatalytic activity of Zr$_2$Cu was in good agreement with the already analyzed PL, DRS and PXRD results. Fig. 19a represents the spectral absorbance of Zr$_2$Cu NCO under Sunlight illumination. The rate constants for ZrO$_2$, CuO, ZrCu, ZrCu$_2$ and Zr$_2$Cu was calculated by plotting ln C/C$_0$Vs illumination time as shown in Fig. 19c and found to be 4.3, 3.2, 4.09, 2.38 and 11.19*10^{-4} min^{-1} respectively.

3.11.4. Photocatalytic mechanism

The photocatalytic mechanism mainly occurs due to the following factors such as (i) the light absorption of the sample, (ii) the production of charge carriers (electrons and holes), (iii) the transfer of charge carriers, and (iv) the utilization of charge carriers by
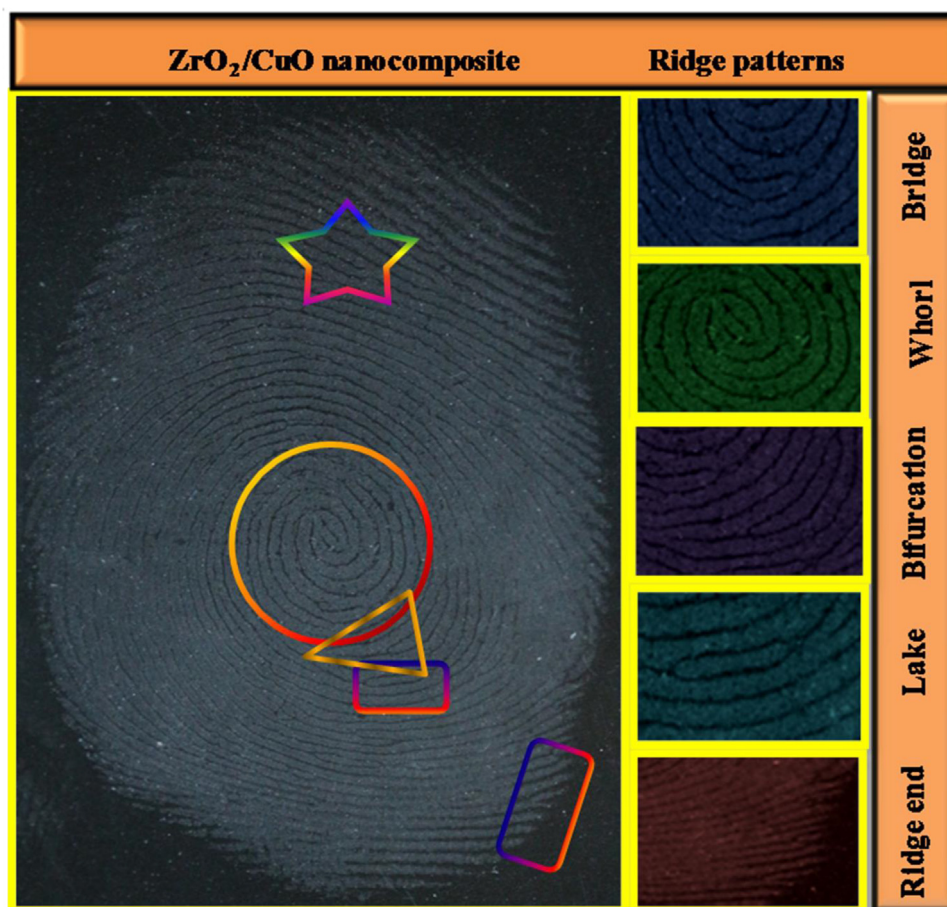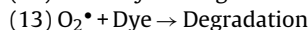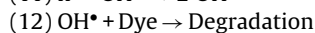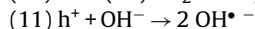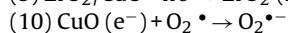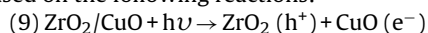
Fig. 17. LFP stained by ZrO$_2$/CuO NCO (left) and some minutia ridges of the latent fingerprint were identified and images were shown (right).

the reactants. When Sunlight falls on the photocatalyst, the electrons jump from the valence band of ZrO$_2$ and CuO to conduction band leaving behind the same number of holes in the corresponding valence band positions. As the E$_{cb}$ value of ZrO$_2$ (−1.14) was more negative compared to E$_{cb}$ value of CuO (0.4), the electrons moves from the CB of ZrO$_2$ to CB of CuO. In the meanwhile, the holes will migrate in the opposite direction from valence band of CuO to valence band of ZrO$_2$ (Fig. 20).The mechanism can be explained based on the following reactions:

(9) $ZrO_2/CuO + h\upsilon \rightarrow ZrO_2\,(h^+) + CuO\,(e^-)$

(10) $CuO\,(e^-) + O_2{}^\bullet \rightarrow O_2{}^{\bullet -}$

(11) $h^+ + OH^- \rightarrow 2\,OH^{\bullet\,-}$

(12) $OH^\bullet + Dye \rightarrow Degradation$

(13) $O_2{}^\bullet + Dye \rightarrow Degradation$

The electrons produced react with atmospheric oxygen and produce superoxide radical (O$_2{}^{\bullet-}$). The holes present in the valence band will react with water molecules to produce hydroxyl radical (OH$^\bullet$). This formation of radicals will be very much helpful to avoid electron-hole pair recombination efficiently and enhance the photocatalytic activity. These formed radicals will attack the dye molecules, breakdown the bonds and degrade it completely.

To determine the key role player in the photocatalytic mechanism, out of the three components namely, holes, electrons and the generated radicals (OH$^\bullet$), a suite of trapping experiment was conducted as depicted in Fig. 19e. In order to conduct this trapping experiment, 1 mM of ethanol (EtOH), isopropyl alcohol (IPA) and AgNO$_3$ solutions were used. When 1 mM of EtOH was added to trap the holes, the% degradation was decreased abruptly to 30%, while 1 mM of IPA addition to trap the hydroxyl radical (•OH) reduces the percentage of degradation to 45%. Finally, 1 mM of AgNO$_3$ was

added to trap the electrons, there was found to be an increase in the percentage degradation to 98%. From the above inference, it is clear that in photocatalytic mechanism, holes are the key role players. These holes will easily react with the hydroxyl ions by breaking down the bonds and degrade it completely. The next major role was played by the hydroxyl radical (•OH) that will effectively degrade the dye molecules.

3.11.5. Stability of photocatalyst

The stability of the photocatalyst was also very important in photocatalysis. The cyclic experiments were conducted for five cyclic runs of Zr$_2$Cu photocatayst as depicted in Fig. 19d. After the first cycle, the photocatalyst was washed with deionized water, dried and used for next cyclic run. The same photocatalyst was added to freshly prepared dye solution. The above said procedure was repeated for all the cyclic runs. The degradation percentage was almost found to be same till fourth cycle and after that a very small decrease was observed in percentage of degradation which may be due to the loss of photocatalyst while washing. The photocatalyst was found to be photostable and can be reused efficiently.

3.11.6. Photodegradation of other dyes

The photocatalyst Zr$_2$Cu was tested for different types of dyes such as Rhodamine B (RhB), Methylene Blue (MB), Direct green (DG) and IC under Sunlight illumination for about one hour. The initial concentration of dye was kept constant and the same procedure used for degradation of IC dye was adopted for all the dyes. It is seen from Fig. 19f, that all the dyes have showed degradation above 75%, which proves the potential of synthesized NCO.
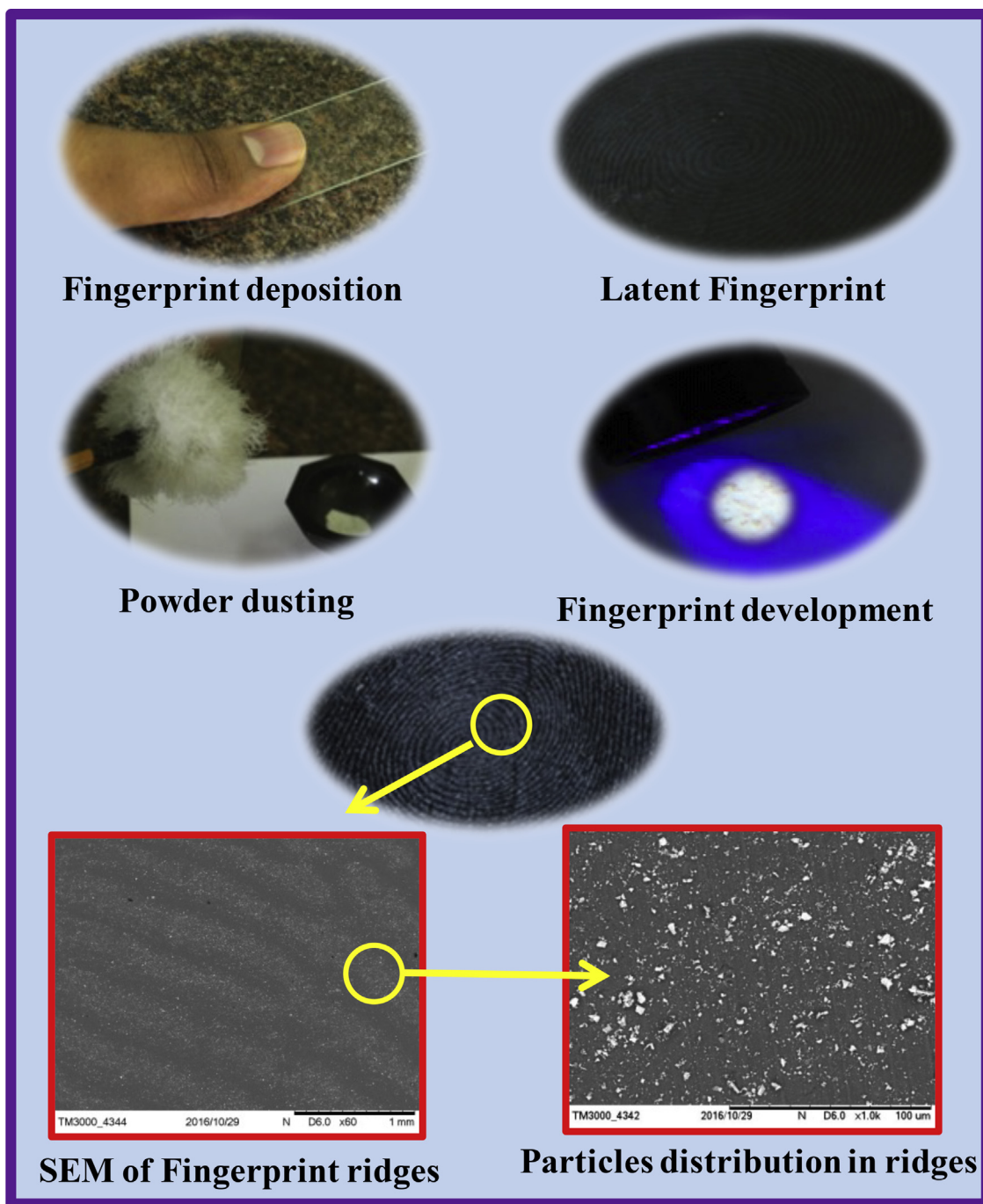
Fig. 18. Pictorial representation for enhancement of LFPs using Zr_2Cu NCO photocatalyst by dusting process & SEM image of Zr_2Cu NCO for clear observation of fingerprint ridges and particle distribution in ridges.

4. Conclusions

To the best of our knowledge, this is the first time a simple synthetic method is employed for the preparation of ZrO_2/CuO NCO photocatalysts. The novelty of this technique lies in its simplicity and the capability of production of NCO's by quick process and does not require any elaborate setup. Here, we have reported simple combustion method for the preparation of ZrO_2, CuO NPs and ZrO_2/CuO NCO's with various compositions of CuO as metal nitrates. By employing this method, a good separable nanocomposite photocatalyst obtained by tailoring the compositions of ZrO_2/CuO NCO. The PXRD pattern of NCO's exhibits the phases corresponding to both ZrO_2 and CuO hence proving the forma-

tion of NCO's. The unique optical property, PL analysis, CIE and CCT indicates that the present NCO is an effective blue component in WLED's. The synthesized Zr_2Cu composite exhibited excellent photocatalytic activity towards the degradation of various dyes under Sunlight. This can be ascribed to the fewer re-combinations of photo-generated carriers in the NCO system. It is believed that, these materials will find promising applications in the field of catalysis particularly waste water treatment. Zr_2Cu NCO with high photocatalytic and high photoluminescence can also be employed as labeling agent to enhance LFPs on different surfaces. The developed LFPs is facile with high sensitivity, low background, high efficiency and can adhere well on different surfaces that helps in developing LFPs in forensic applications. It has been demonstrated
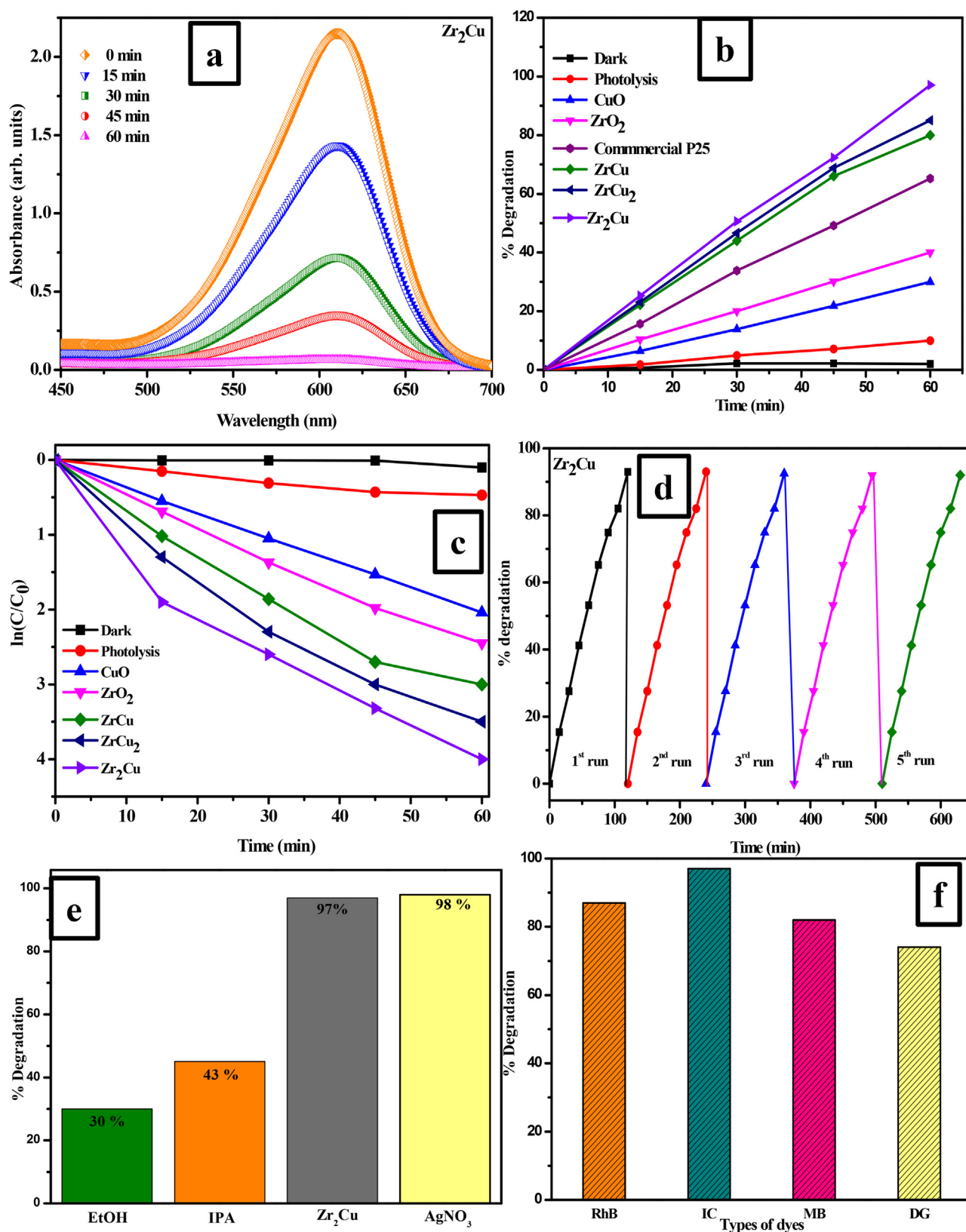
Fig. 19. (**a**) Spectral absorbance of Zr_2Cu NCO with the variation of illumination time under Sunlight for degradation of IC dye (**b**) % degradation of IC under Sunlight illumination for ZrO_2, CuO NPs and ZrO_2/CuO NCO's (**c**) Plot of ln (C/C_0) versus illumination time for the degradation of IC dye under Sunlight illumination for ZrO_2, CuO NPs and ZrO_2/CuO NCO's (**d**) Reusability of Zr_2Cu photocatalyst for five consecutive recycle runs (**e**) Photocatalytic degradation of IC using different radical scavengers over Zr_2Cu photocatalyst under Sunlight illumination (**f**) Application of Zr_2Cu photocatalyst for degradation of various dyes under Sunlight illumination.
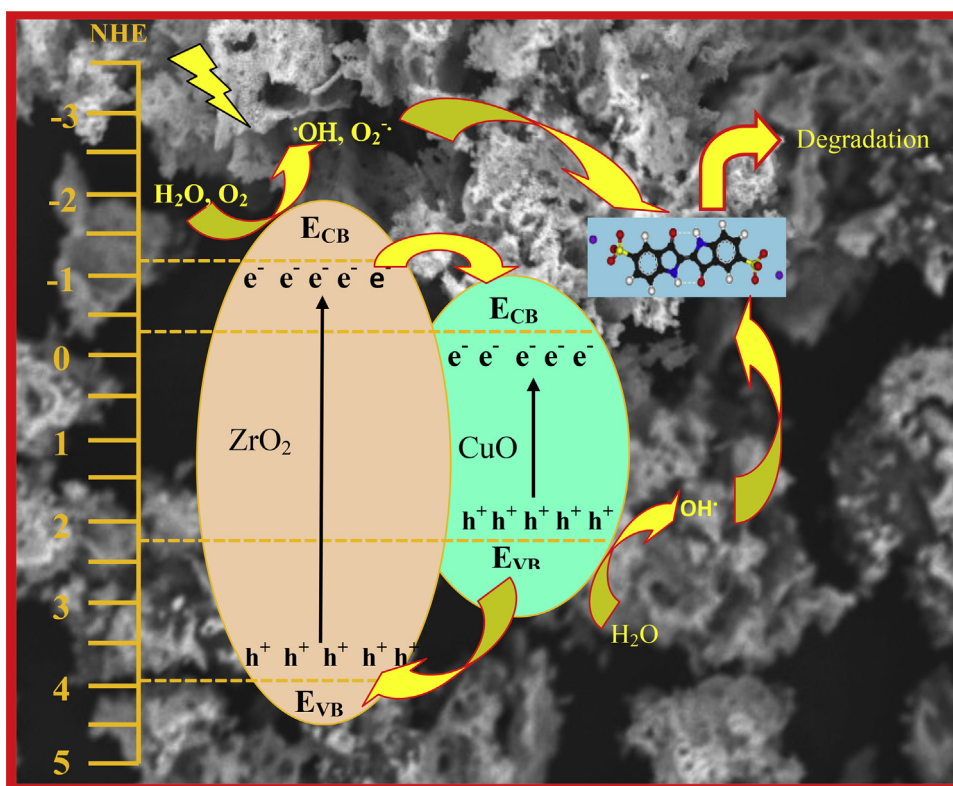
Fig. 20. Mechanism for the photocatalytic degradation of IC dye under Sunlight illumination.

that its capability to act as a multifunctional material as excellent photocatalytic activity towards degradation of various dyes under Sunlight illumination, effective blue component in display applications as well as a labeling agent to enhance latent fingerprints.

Appendix A. Supplementary data

Supplementary data associated with this article can be found, in the online version, at http://dx.doi.org/10.1016/j.apcatb.2017.03.055.

References

[1] H.L. Huang, Y.Y. Chang, J.C. Weng, Y.C. Chen, C.H. Lai, T.M. Shieh, Thin Solid Films 528 (2013) 151–156.
[2] R. Jayakumar, R. Ramachandran, P.T.S. Kumar, V.V. Divyarani, S. Srinivasan, K.P. Chennazhi, H. Tamura, S.V. Nair, Int. J. Biol. Macromol. 49 (2011) 274–280.
[3] K. Maeda, T. Takata, M. Hara, N. Saito, Y. Inoue, H. Kobayashi, K. Domen, J. Am. Chem. Soc. 127 (2005) 8286–82867.
[4] I. Tsuji, H. Kato, H. Kobayashi, A. Kudo, J. Am. Chem. Soc. 126 (2004) 13406.
[5] A. Fujishima, T.N. Rao, D.A. Tryk, J. Photochem. Photobiol. C 1 (2000) 1–21.
[6] X.B. Chen, S.H. Shen, L.J. Guo, S.S. Mao, Chem. Rev. 110 (2010) 6503–6570.
[7] K. Mori, H. Yamashita, M. Anpo, RSC Adv. 2 (2012) 3165–3172.
[8] W. Choi, A. Termin, M.R. Hoffmann, J. Phys. Chem. 98 (1994) 13669–13679.
[9] R. Ashi, T. Morikawa, T. Ohwaki, K. Aoki, Y. Taga, Science 293 (2001) 269–271.
[10] G.H. Qin, Z. Sun, Q.P. Wu, L. Lin, M. Liang, S. Xue, J. Hazard. Mater. 192 (2011) 599–604.
[11] D. Zhang, Transit. Met. Chem. 35 (2010) 689–694.
[12] D. Zhang, F. Zeng, Appl. Surf. Sci. 257 (2010) 867–871.
[13] Z.H. Zhang, Y. Yuan, Y.J. Fang, L.H. Liang, H.C. Ding, L.T. Jin, J. Talanta 73 (2007) 523–528.
[14] C. Wang, X.M. Wang, B.Q. Xu, J.C. Zhao, B.X. Mai, P.A. Peng, G. Sheng, J. Fu, J. Photochem. Photobiol. A 168 (2004) 47–52.
[15] S. Sakthivel, S.U. Geissen, D.W. Bahnemann, V. Murugesan, A. Vogelpohl, J. Photochem. Photobiol. A 148 (2002) 283–293.
[16] D. Li, H. Haneda, J. Photochem. Photobiol. A 160 (2003) 203–212.
[17] N. Chandra, D.K. Singh, M. Sharma, R.K. Upadhyay, S.S. Amritphale, S.K. Sanghi, J. Colloid Interface Sci. 342 (2010) 327–332.
[18] L.Y. Zhu, X.Q. Wang, G.H. Zhang, Q. Ren, D. Xu, Appl. Catal. B 103 (2011) 428–435.
[19] Y. Li, Q. Fu, M. Flytzani- Stephanopoulos, Appl. Catal. B 27 (2000) 179–191.
[20] S. Hilaire, X. Wang, T. Luo, R.J. Gorte, J. Wagner, Appl. Catal. A 215 (2001) 271–280.
[21] X. Wang, J.C. Hanson, J.A. Rodriguez, D. Gamarra, A. Martinez Arias, M. Fernandez-Garcia, J. Phys. Chem. B 110 (2006) 428–434.
[22] H. Kusar, S. Hocevar, J. Levec, Appl. Catal. B 63 (2005) 194–200.
[23] T. Tabakova, F. Boccuzzi, M. Manzoli, J.W. Sobczak, V. Idakiev, D. Andreeva, Appl. Catal. A 298 (2006) 127–143.
[24] B.M. Reddy, A. Khan, Catal. Rev. 47 (2007) 257–296.
[25] A. Burri, N. Jiang, S.E. Park, Catal. Sci. Technol. 2 (2012) 514–520.
[26] B. Neppolian, Q. Wang, H. Yamashita, H. Choi, Appl. Catal. A 333 (2007) 264–271.
[27] Abdullah M. Alotaibi, Sanjayan Sathasivam, Sean P. Nairc, Ivan P. Parkin, J. Mater. Chem. B 4 (2016) 666–671.
[28] Yan Jian-Hui, Yao Mao-Hai, Zhang Li, Tang You-Gen, Yang Hai-Hua, J. Cent. South Univ. Technol. 18 (2011) 56–62.
[29] Muhammad Ali Ehsan, Abbas Saeed Hakeem, Hamid Khaledi, Muhammad Mazhar, Muhammad Mehmood Shahid, Alagarsamy Pandikumar, Nay Ming Huang, RSC Adv. 5 (2015) 103852–103862.
[30] Yan Jian-hui, Yao Mao-hai, Zhang Li, Tang You-gen, Yang Hai-hua, J. Cent. South Univ. Technol. 18 (2011) 56–62.
[31] W. Lin, H. Frei, J. Am. Chem. Soc. 127 (2005) 1610–1611.
[32] J. Yin, Z.G. Zou, J.H. Ye, J. Phys. Chem. B 107 (2003) 4936–4971.
[33] P. Sathishkumar, R. Sweena, J. Wu. Jerry, S. Anandan, J. Chem. Eng. 171 (2011) 136–140.
[34] B. Neppolian, Q. Wang, H. Yamashita, H. Choi, Appl. Catal. A 333 (2007) 264–271.
[35] W. Liao, T. Zheng, P. Wang, S. Tu, W. Pan, J. Environ. Sci. 22 (2010) 1800–1806.
[36] A.K.L. Sajjad, S. Shamaiila, B.Z. Tian, F. Chen, J.L. Zhang, J. Hazard. Mater. 177 (2010) 781–791.
[37] N. Couselo, F.S.G. Einschlag, R.J. Candal, M. Jobbagy, J. Phys. Chem. C 112 (2008) 1094–1100.
[38] L. Yang, Y. Xiao, S. Liu, Q. Cai, S. Luo, G. Zeng, Appl. Catal. B 94 (2010) 142–149.

[39] W. Smith, Y.P. Zhao, Catal. Commun. 10 (2009) 1117–1121.
[40] Fa-tang Li, Gab Jingrun Ran, Gb. Mietek Jaroniec, Shi Zhang Qiao, Nanoscale 7 (2015) 17590–17610.
[41] W. Wena, Jin-Ming Wu, RSC Adv. 4 (2014) 58090–58100.
[42] Arvind Varma, Alexander S. Mukasyan, Alexander S. Rogachev, Khachatur V. Manukyan, Chem. Rev. 116 (23) (2016) 14493–14586.
[43] G.P. Darshan, H.B. Premkumar, H. Nagabhushana, S.C. Sharma, B. Daruka Prasad, S.C. Prashantha, R.B. Basavaraj, J. Alloys Compd. 686 (2016) 577–587.
[44] B. Yu, X.L. Li, L. Zhang, Yu. Zhang, T.T. Wang, L. Li, C.G. Wang, Z.M. Su, Dyes Pigm. 134 (2016) 178–185.
[45] L.K. Seah, U.S. Dinish, W.F. Phang, Z.X. Chao, V.M. Murukeshan, Forensic Sci. Int. 152 (2005) 249–257.
[46] Arvind Varma, Alexander S. Mukasyan, Alexander S. Rogachev, Khachatur V. Manukyan, Chem. Rev. 116 (23) (2016) 14493–14586.
[47] M.N. Tahir, L. Gorgishvili, Jixue Li, T. Gorelik, U. Kolb, L. Nasdala, W. Tremel, Solid State Sci. 9 (2007) 1105–1109.
[48] E.D. Sherly, J. Judith Vijaya, N. Clament Sagaya Selvam, L. John Kennedy, Ceram. Int. 40 (2014) 5681–5691.
[49] K. Giannousi, I. Avramidis, C. Dendrinou-Samara, RSC Adv. 3 (2013) 21743–21752.
[50] Y.S. Vidya, K. Gurushantha, H. Nagabhushana, S.C. Sharma, K.S. Anantharaju, C. Shivakumara, D. Suresh, H.P. Nagaswarupa, S.C. Prashantha, M.R. Anilkumar, J. Alloys Compd. 622 (2015) 86–96.
[51] M.R. Anilkumar, H.P. Nagaswarupa, K.S. Anantharaju, K. Gurushantha, C. Pratapkumar, S.C. Prashantha, T.R. Shashi Shekhar, H. Nagabhushana, S.C. Sharma, Y.S. Vidya, Daruka Prasad, Mater. Res. Express 2 (2015) 035011.
[52] L. Renuka, K.S. Anantharaju, S.C. Sharma, H.P. Nagaswarupa, S.C. Prashantha, H. Nagabhushana, Y.S. Vidya, J. Alloys Compd. 672 (2016) 609–622.
[53] J. Jayaprakash, N. Srinivasan, P. Chandrasekaran, E.K. Girija, 136 (2015) 1803–1806.
[54] R. Sharma, B. Paul, P. Banerji, Appl. Surf. Sci. 256 (2010) 2232–2235.
[55] X. Hou, X. Wang, B. Liu, Q. Wang, Z. Wang, D. Chen, G. Shen, ChemElectroChem 1 (2014) 108–115.
[56] Mingjin Li, Aiping Li, Haiqing Xu, Liangdong Feng, Int. J. Electrochem. Sci. 10 (2015) 4405–4415.
[57] Guorong Duan, Chunxiang Zhang, Aimei Li, Xujie Yang, Lude Lu, Xin Wang, Res. Nanoscale Lett. 3 (2008) 118–122.
[58] Weimin Dua, Zhaoqiang Zhu, Xiaofen Zhang, Dacheng Wanga, Donghe Liu, Xuefeng Qian, Jimin Dua, Mater. Res. Bull. 48 (2013) 3735–3742.
[59] S. Wright, R.C. Barklie, Mater. Sci. Semicond. Process 9 (2006) 892–896.
[60] C. Gionco, M. Cristina Paganini, E. Giamello, R. Burgess, C. DiValentin, G. Pacchioni, Chem. Mater. 25 (2013) 2243–2253.
[61] K.V. Chary, G.V. Sagar, D. Naresh, K.K. Seela, B. Sridhar, J. Phys. Chem. B 109 (2005) 9437–9444.
[62] L. Zhu, M. Hong, G.W. Ho, Nano Energy 11 (2015) 28–37.
[63] L.C. Wang, Q. Liu, M. Chen, Y.M. Liu, Y. Cao, H.Y. He, K.N. Fan, J. Phys. Chem. C 111 (2007) 16549–16557.
[64] A.A. Ballman, S.P.S. Porto, A. Yariv, J. Appl. Phys. 34 (11) (1963) 3155–3156.
[65] Norzahir Sapawe, New J. Chem. 39 (2015) 4526–4533.
[66] Miguel Pelaez, Nicholas T. Nolan, Suresh C. Pillai, Michael K. Seery, Polycarpos Falaras, Athanassios G. Kontos, Patrick S.M. Dunlop, Jeremy W.J. Hamilton, J. Anthony Byrne, Kevin O'shea, Mohammad H. Entezari, Dionysios D. Dionysiou, Appl. Catal. B: Environ. 125 (2012) 331–349.
[67] Yong Xu, Martin A.A. Schoonen, Am. Mineral. 85 (2000) 543–556.
[68] D.E. Pacheco-Catalán, Mascha A. Smit, E. Morales, Int. J. Electrochem. Sci. 6 (2011) 78–90.
[69] F.F. Santiago, G.G. Belmonte, J. Bisquert, A. Zaban, P. Salvador, J. Phys. Chem. B 106 (2002) 334–339.
[70] Pankaj Yadav, Kavita Pandey, Parth Bhatt, Brijesh Tripathi, Manoj Kumar Pandey, Manoj Kumar, Mater. Sci. Eng. 206 (2016) 22–29.
[71] Divinah Manoharan, Aswaghosh Loganathan, Vishista Kurapati, Victor Jaya Nesamony, Ultrason. Sonochem. 23 (2015) 174–184.
[72] K. Joy, J.I. Berlin, P.B. Nair, J.S. Lakshmi, G.P. Daniel, P.V. Thomas, J. Phys. Chem. Solids 72 (2011) 673–677.
[73] J. Liopis, Phys. Status Solidi A 119 (1990) 661–667.
[74] G. Lucoysky, C.L. Hinkle, C.C. Fulton, N.A. Stoute, H. Seo, J. Luning, Radiat. Phys. Chem. 75 (2006) 2097–2101.
[75] A. Emeline, G.V. Kataeva, A.S. Litke, A.V. Rudakova, V.K. Ryabchuk, N. Serpone, Langmuir 14 (1998) 5011–5022.
[76] N.C.S. Selvam, J.J. Vijaya, L.J. Kennedy, Ind. Eng. Chem. Res. 51 (2012) 16333–16345.
[77] J. Liqiang, Q. Yichun, W. Baiqi, et al., Sol. Energ. Mat. Sol. Cells 90 (12) (2006) 1773–1787.
[78] Damian Wojcieszak, Danuta Kaczmarek, Jaroslaw Domaradzki, Michal Mazur, Int. J. Photoenergy 20 (13) (2013) 526140 (cite this article:).
[79] J.C. De Mello, H.F. Wittmann, R.H. Friend, Adv. Mater. 9 (1997) 230–232.
[80] L.O. Palsson, A.P. Monkman, Adv. Mater. 14 (2002) 757–758.
[81] P.K. Jisha, Ramachandra Naik, S.C. Prashantha, H. Nagabhushana, S.C. Sharma, H.P. Nagaswarupa, K.S. Anantharaju, B. Daruka Prasad, H.B. Premkumar, J. Lumin. 163 (2015) 47–54.
[82] M. Vijayakuma, K. Marimuthu, J. Alloys Compd. 629 (2015) 230–241.
[83] Zhenghua Fan, Fanming Meng, Miao Zhang, Zhenyu Wu, Zhaoqi Sun, Aixia Li, Appl. Surf. Sci. 360 (2016) 298–305.